2D Spectroscopy in Astronomy

Bachelor Thesis
Joona Rautiainen
Faculty of Natural Sciences
University of Oulu
Spring 2019

Abstract

2D-spectroscopy in astronomy is defined as a technique where a spatially resolved electromagnetic spectrum is obtained over a two-dimensional field. In this paper the very basic principles of spectroscopy are briefly covered starting from the single slit concept via the Huygens principle and the Fraunhofer diffraction. The basic concept of a grating-based spectrograph is described. The connection between observed spectra, the chemical footprints and the underlying physical properties of the systems are briefly covered. The main IFU techniques used in the field of integral field spectroscopy are introduced. The basic ideas on how the data from the observed targets are produced and the wanted physical properties from the data are recovered are discussed. The work demonstrates the usage of 2D-spectroscopic data and its usefulness. The decay in the velocity dispersion profiles in the near central regions of galaxies known as sigma-drop is briefly introduced and a sample of 13 galaxies hosting a possible sigma-drop is analyzed via elliptical apertures. The radial profiles of each galaxy are extracted from given 2D-data connected to the kinematics of the sample galaxies. The radial profiles are then graphically presented with kinematic maps corresponding to the rotation velocity, the velocity dispersion, h_4 and h_3 profiles of the galaxy. Here the h_4 and h_3 are the amplitudes of the Gauss-Hermite series corresponding to the symmetric and asymmetric deviation from a Gaussian. The sample consists of only barred galaxies which could indicate star formation caused sigma-drops due to the bar-driven inflow of the gas to the central regions of the galaxies. Well-defined dust lanes are seen in $\approx$70% of the sample showing a possible relation between the dust and the sigma-drops. There is no direct connection observed between the sigma-drops and the sizes of the galaxies.

Contents

1 Introduction

In music we have notes which correspond to different frequencies that are combined in different manners to form scales. Notes in scales are then used to construct a melody that one can hear as a story. In a similar manner in spectroscopy a wave of light with a certain frequency can be connected to a typical atom or molecule (forming a chemical trace that can be recognized). The light can be emitted, absorbed and scattered by particles. By locating these characteristic "spectral-notes" within the spectrum the connection between the physical environment and the particles in it can be derived. As spectra consist of multiple light frequencies ("spectral-notes") it is a measure of received photons with certain energies. In the spectrum the abundances of the chemicals in it are related to the intensities of the measured "spectral-notes" thus telling a "story" of the environment.

In astronomy it is often not possible to do a voyage where one is in a physical contact with the object. Instead the electromagnetic radiation observed from different systems can be used to form the best possible description of the physical and chemical properties of the targets. This should not be taken as a disadvantage but as a possibility. Electromagnetic radiation carrying the information across the vast space, with a limited speed, opens a window for gazing into the past allowing observation of objects in the very beginning of their lifetime. As most of the information that is within radiation is too faint to be extracted with a naked eye or outside the sensitivity range of the eye the need for tools to extract the information is justified. Long-slit spectroscopy has pioneered the field of the work by unveiling the rotating nature of many galaxies among other things. However as the research of the universe proceeds the limitations of this technique have shown a need for a tool that can simultaneously obtain the spectral coverage connected to a specific location in the sky. 2D-spectroscopy is the tool in astronomy to trace these chemical and physical footprints by simultaneously connecting the observed spectrum and the sampled area in the sky. The data from the target can be later reconstructed as a map containing the spatially resolved spectra.

In this work the technique called 2D-Spectroscopy in astronomy is introduced. The technique is also demonstrated with a velocity dispersion decay phenomena in the central regions of galaxies called σ-drop. The 2nd section is meant to cover the basic information about 2D-spectroscopy ranging from the basic idea of spectroscopy connected to the basic principles of tracing chemical and physical footprints to the techniques used in the field to obtain the wanted spectra. In the 3rd section actual 2D-spectroscopic data are used to demonstrate the techniques in use through kinematic maps of galaxies and by further analyzing the data by extracting the radial velocity

dispersion profiles for a sample of 13 galaxies.

2 2D - Spectroscopy

2.1 Brief theory

2.1.1 Spectroscopy

The Huygens principle states that a wavefront of light can be described to compose of points of spherical wavelets rising from a prior instant of the advancing wave. When a wavefront enters through a slit with a width of a the light from each point source ends up travelling different distances to point a x that is seen at an angle θ off of the optical axis at distance D. As the waves arrive to the same locations with different phases (due to the distances travelled) the superposition of these wavelets can been seen as diffraction pattern. The minimum indices for a monochromatic light can be found at angle θ from

$$a \sin\theta = m\lambda \tag{1}$$

where the a is width of the slit, λ is the wavelength and m is an integer. This basic idea of the single slit diffraction is shown in Figure 1. If the angles are relatively small one can say that $\theta \approx x/D$ where x is position of the minimum from the optical axis.

The intensity of the light at an angle θ is given by the Fraunhofer diffraction equation

$$I(\theta) = I_0 \frac{\sin^2(\pi\alpha)}{(\pi\alpha)^2},\ \alpha = \frac{a\sin\theta}{\lambda} \tag{2}$$

where I_0 is the intensity at $\theta = 0$. While having multiple slits instead of one the resulting wave fronts will interfere constructively and destructively. With N slits with an equal separation d the intensity $I(\theta)$ for zero width slit is given by

$$I(\theta) = I_0 \frac{\sin^2(N\pi\beta)}{(\pi\beta)^2},\ \beta = \frac{d\sin\theta}{\lambda} \tag{3}$$

where the d is distance between the slits. Combining the effects on these two yield a interference pattern with a single slit envelope expressing the finite width of the slits. The resulting intensity is given as

$$I(\theta) = I_0 \frac{\sin^2(N\pi\beta)}{(\pi\beta)^2} \frac{\sin^2(\pi\alpha)}{(\pi\alpha)^2} \tag{4}$$

this can be said to be the basic principle of spectroscopy. [1]

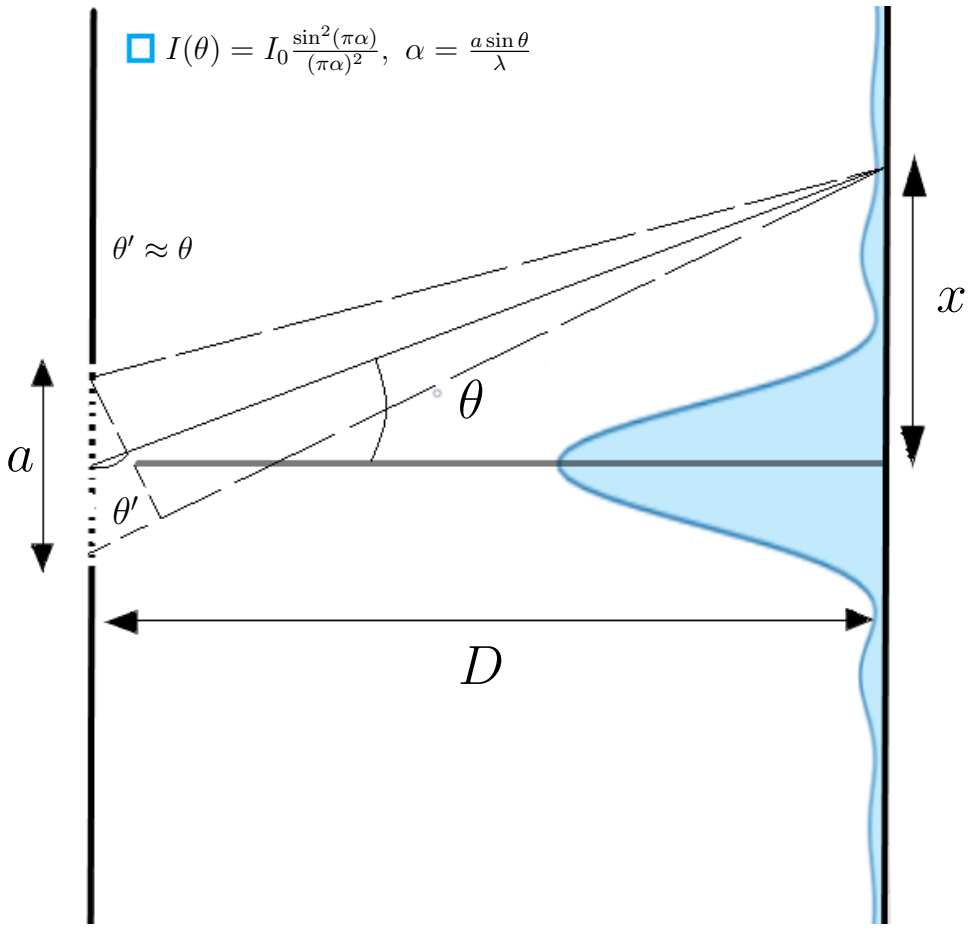

Figure 1: A single slit diffraction where the intensity I_θ is shown for the values of α in the range $[-\pi, \pi]$. Concept: HyperPhysics (HP)

The observed light consists of many photons with different energies so for many purposes it is useful to separate the incident wave into multiple waves with a spectrograph. The separation can be done by a grating or a prism. The basic structure of a spectrograph is formed by a slit turning the incident light into parallel light which is then dispersed by a grating or a prism onto a camera that focuses the parallel-dispersed incident light onto a detector. The used slit width partially determines the resolution of the spectrograph by regulating the amount of light directed to the diffraction phase. The increasing photon count can make the system operate faster but the minimum wavelength difference that can be resolved increases. The later section shows that the slit can be replaced with pseudo-slit allowing a faster throughoutput. The wavelength seen by the detector is then given by the angle α of the incident wave and the angle β of the outgoing beam relative to the normal of the grating instrument.

$$m\lambda = d(\sin\alpha + \sin\beta) \tag{5}$$

where the m is an integer indicating the order in use and d is the distance between grating elements. The maximum efficiency angle for a particular $m\lambda$ is called the blaze angle. Since there is possibility for overlapping, for example light at $\lambda = 6000$Å and second order from $\lambda = 3000$Å, some systems use filtering after the slit phase to get rid of unwanted wavelengths. The spectral resolution is given by the ability of the spectrograph to resolve features in the spectra and its usually defined as

$$R = \frac{\lambda}{\Delta\lambda} \tag{6}$$

where λ is the wavelength of the electromagnetic radiation and $\Delta\lambda$ the smallest feature that can be distinguished from the produced spectra. [2]

2.1.2 Characteristic radiation

The separated electromagnetic radiation then forms the spectra. The colors in the spectra are connected with the energies of the photons. The energy of electromagnetic radiation with frequency ν is given by

$$E = h\nu \tag{7}$$

where h is the Planck constant. An excited atom emits a photon when relaxing to the lower energy state E_i (the energy transfer can be done by other means for example through Auger emission). The energy difference between these levels corresponds to the energy of the photon emitted. The

same principle applies for absorption where the energy is used to excite the atom to a higher energy state. The energy difference of the initial E_i and the final state E_f corresponds to the energy of the interaction. The energy correlated to observed photon absorption is

$$|E_i - E_f| = \Delta E = h\nu \tag{8}$$

Since different atoms are made of different number of protons, neutrons and electrons the potential that a electron experiences in the neighbourhood of the parent atom varies between atoms. The available energy states for the electron to access and the ionization energies of the atoms are then characteristic for individual elements. These characteristic energies are then used to trace the chemical footprints of the system.

On the other hand if we know the chemicals, for example comparing the observed spectra to reference spectra and find a match, the energies involved can be used to describe the physical nature of the target. This can be demonstrated with the Doppler effect. A particle moving towards the observer emits a photon with a frequency ν this photon is then received with a frequency ν'. The corresponding velocity of the particle relative to the observer is given by

$$v = \frac{\nu - \nu'}{\nu} c \tag{9}$$

where the c is the speed of light and $v << c$ is assumed. [3]

2.1.3 Spectroscopy and Astronomy

Stars can be thought to be black-bodies that absorb and emit electromagnetic radiation accordingly. By observing the spectra from a single star certain physical elements can be extracted from the deviations from a black-body spectra. The energy of a photon absorbed in the atmosphere of a star can be connected to the chemical composition (as the atmosphere represents the initial composition values of the star) and by comparing the intensities of the absorption to the continuum in the atmosphere the abundances can be derived. Of course the same applies to the observed emission lines. [4] From the known chemical composition a spectral classification of stars is done (as in the Henry Draper (HD) classes of Edward Pickering that are formed from the characteristic spectral features observed within stellar spectra) to describe stars within a stellar population.

Stars produce heavy elements through fusion and then redistribute them to the surroundings enriching the next population of stars with heavy elements. The rate and properties of the chemicals distributed depends on

things such as available gas (as gas density affects the star formation rate (SFR)), the number distribution of the stars born with a given mass interval (initial mass function (IMF) affecting the elements released to the surroundings) and the dynamical environment of the system (as the star formation is linked to the dynamical evolution). The abundances of heavy elements (or metals that are often considered as everything heavier than H and He in astronomy) with kinematics and ages in a stellar system can be then used to determine the underlying stellar populations by modelling the observed spectral information with stellar libraries and theoretical models that include different IMF, SFR and possible dynamical aspects. The stellar populations can be divided into Population I, Population II and Population III where the first corresponds to stars that have relatively high metallicity and are young (the Sun for example), the second has considerably lower metallicity and the third represent the population where basically no metals would be observed. By knowing the chemical composition of the population certain physical aspects of the system can be derived just by looking the spectra such as distinguishing differences between halo, bulge and disk stars in a galaxy. [5]

The broadening of a spectral line itself can tell much about the system. In dense gas there are frequent collisions between the particles that affect the width of the observed spectra with collisional broadening. The collisional broadening due to the particle interactions in a system can be described as an increase in the Heisenberg uncertainty principle by affecting the time domain which gives rise to a Lorenzian like line profile. The time that an atom spends in an excited state is affected by the collisions which then increases the uncertainty resulting broader observed profile. The effect can be related to the temperature as well as the density of the gas in a system. For example in cool low-density regions the collision broadening in a line profile will not play a role because of the times between collisions are much longer than the time needed for the excited atom to emit the photon and return to ground state and thus is practically only affected by the natural broadening of the uncertainty principle. On the other hand if the temperature of the gas increases the time between the collisions decreases increasing the uncertainty leading to a larger broadening in a observed line profile.

In a system where the particles are moving with a Maxwellian velocity distribution the observed spectra are affected by the thermal broadening which is shown as a Gaussian like line profile.

The observed spectral lines can be fitted with these profiles (or to the sums or products of these functions) to model certain spectral lines in order to obtain the physics behind the line profiles that are described. As this is the case for gas (as it can be thought to be combination of the Lorenzian

and Gaussian line profiles) cause the spectral line follow a Voigt like profile corresponding to the random motions and collisions between the gas particles. The stars in a galaxy can be thought as non-collisional particles that interact with each other through gravitation. As stars can be thought as collision-free the key role of spectral broadening of a stellar system is due to the heat of the system. [6] [7]

2.1.4 On the stellar dynamics

By analyzing the different spectral lines in different parts of the system one can derive the rotation velocity of the system and the velocity dispersion. In a larger system such as galaxy the gas has more rotation-favored velocity than the stars while stars show more dispersion in the measured velocities (even though stars in disk galaxies can also have high rotation velocities compared to the velocity dispersion).

Let's assume that we have a concentration of gas with a centrally concentrated mass distribution (as observed for gas and baryons) that has a favored rotation direction around one axis. This means that in the direction of the rotation axis the particles are not affected by the centrifugal force and the configuration flattens. As the gas density is higher at the plane of rotation the gas particles going through the denser plane get "dragged" through gas-gas collisions and the corresponding velocity experiences damping and eventually sets the gas particles on the plane. In galaxies the rotation velocities $v(r)$ profiles are nearly flat which means that the angular velocity $\omega = \frac{v}{r}$ of gas in the systems go as $\propto r^{-1}$. This leads to a differential rotation and friction between clouds. The friction between clouds heats the system and this energy is radiated away. As the gas loses energy it sinks deeper into the potential well and the gas is packed until it reaches a critical density. The pressure of the system is over powered by the gravitation and collapse begins. This results in a dynamically cold new stellar component with an enriched chemical composition. In a very dense region, such as near the galaxy center, the distribution of masses coupled with structures like bars, spiral arms and super-massive molecular clouds or possible merger events will dynamically heat the stars and cause the velocity dispersion broaden over time. Since the this would be done over time it should trace the chemical evolution of the stars showing higher dispersion in older stellar populations while the younger populations should follow the kinematics inherited from the gas.

Observing spectral traces rising from the different components can give dynamical insight of the current system and how it has formed (As the chemical footprints of stars also trace dynamical evolution of the system). Tracing some of the "dynamical-clues", for a better understanding of the system, can

demand a technique where spatial information can be tightly connected to the obtained spectra. [8] [9] [10]

2.2 Definitions

2D-Spectroscopy (often called 3D-spectroscopy or Integral field spectroscopy (IFS) due to the lack of communication between groups that pioneered the methods in 1980s and early 1990s) is an astronomical observing technique where the main goal is to obtain spatially-resolved spectra. The spectra connected to the spatial elements ("spaxels") are obtained simultaneously in a single exposure over a two-dimensional field-of-view (FoV) [11]. The term "spaxel" refers to the spatial elements on the image plane of the telescope that are sampled from the FoV and should be distinguished from pixels that are the the spatial elements in the image plane of the detector. It does not necessarily matter which of the techniques within 2D-spectroscopy is chosen for the task, the output often is a "datacube" with axes of x, y as the spatial axes and wavelength λ forming the third dimension [12]. This is due to the sampling method where each spaxel can be connected to its individual spectrum. Once the spectra has been extracted it is possible to make maps that are reassembled from the wanted wavelengths. For instruments where a orthonormal spatial sampling geometry is applied the spectra can be then rearranged to a 3D-array on the computer to form the so called "datacube".[11] In the datacube one spatial element connected to the spectra is a spaxel and one monochromatic point in a cube is called voxel. This is partly shown in Figure 2.

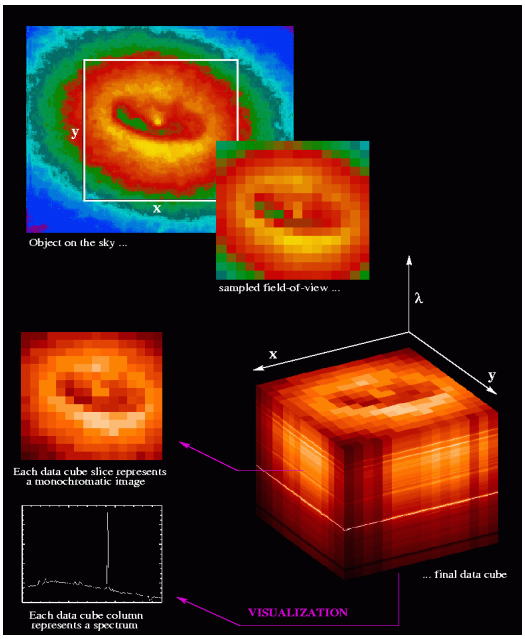

Figure 2: Principle of IFS. Credit: M. Roth 2002

The 2D-devices can be further divided into two categories. Integral field units IFUs that are coupled with spectrograph and Scanning techniques such as Stepped-longslit, Imaging Fourier Transformation Spectroscopy (IFTS) and Fabry-Pérot Interferometry (FPI) that integrate the spectra or spatial

direction over time. All the techniques considered produce a datacube and depending at the research at hand can be thought to work with similar efficiency. For example IFUs might obtain the needed spectra with one exposure but might need several exposures to be combined to get the desired area for analysis. On the other hand technique such as IFTS produce a large area of spaxels with limited spectral range and need the time domain to integrate over the same spectral range as the IFUs. The difference comes in when the techniques are compared in factors such as how the data from different exposures are combined [13].

The long-slit technique introduces problems such as slit losses which occur when electromagnetic radiation with different wavelengths passes through the atmosphere with a differential refraction causing a decrease in flux density received from the target [14] (unless observing at parallactic angle when the refracted light would fall in the slit). As seeing also depends on the wavelength this means that the flux calibrations (for comparison of fluxes between different wavelengths) are affected by systematic errors if the flux standards (reference stars with know properties) are observed through different air masses than the target. For the long-slit absolute flux calibration requires a wider slit to capture all the light resulting lower spectral resolution as a telluric spectrum (spectral features connected to the telluric absorption/emission caused by the chemicals in the atmosphere for example molecular oxygen is seen to absorb solar flux at wavelengths corresponding A and B Fraunhofer lines [4]) must be taken with the same resolution as the main data from the target and thus acquire a separate exposures.

In the IFUs the atmospheric refraction is seen as a shift in the x and y in the datacube but without losses in the received flux. Since all the light is conserved in principle single exposure can be used for both flux and telluric calibration and even differential spectrometry can be performed in case there is a secondary flux standard in the vicinity of the target under observation [11].

Miss-match between the geometry of the object and the slit can also affect the obtained spectra [15]. Things such as the point precision targeting of the object in the slit spectroscopy (while in the IFUs the target can be acquired from the data later on) have made 3D techniques generally preferable to slit spectrometry [13].

2.3 IFUs

The integral field spectrographs have been built based on the different techniques used to sample the FoV into spaxels. Integral field units (IFUs) can be said to be the optical elements that are used to sample the FoV.[11] In

this section three different techniques of IFS on IFU are discussed. The techniques are gathered in Figure 3. The aim of this section is to point out some differences in the in IFS techniques used. The deep theoretical walk through of the aspects in each case would be unnecessary for the scope of this work. The scanning methods are not considered, however, it should be said that the scanning methods are historically the first with motivation to obtain three-dimensional datacube thus worth mentioning. For the reader that is interested in the scanning techniques these are presented in [11].

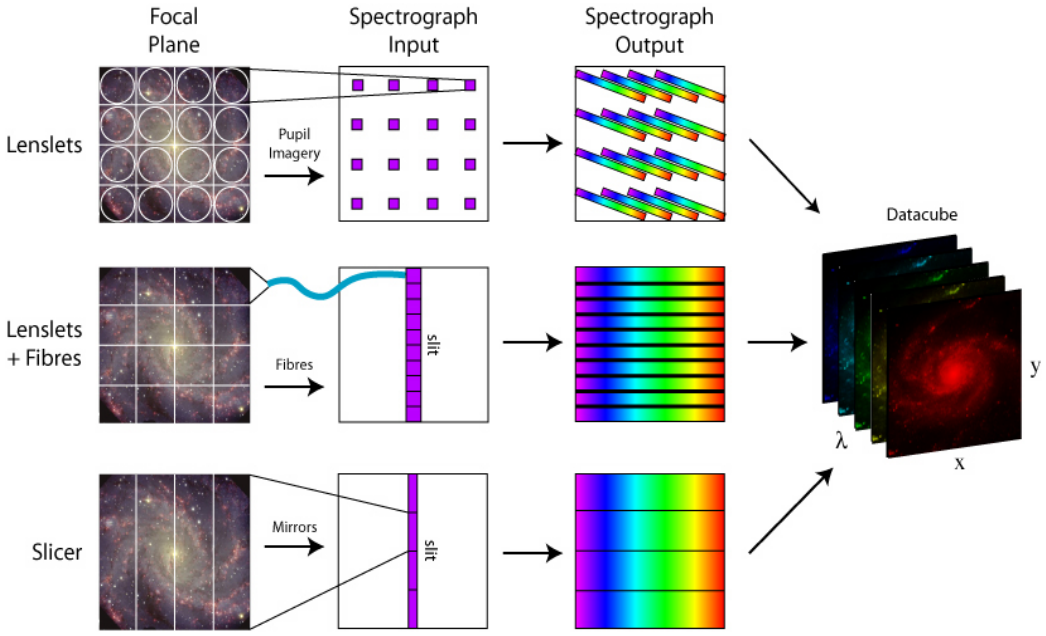

Figure 3: Summary of IFS techniques. Credit: M. Westmoquette, adapted from Allington-Smith et al. 1998

2.3.1 Detectors

For better understanding of the IFU techniques it is useful to briefly go through how these techniques are constrained by the detectors which in the end limit the spatial sampling and wavelength coverage of the instruments. Depending on the research at hand it is often preferable to maximize the number of detectors in a detecting surface in order to obtain the largest field of view (FoV) and spectral coverage. Clearly the packing of information onto a such surface plays a critical role.

Charge coupled device (CCD) is the most common detector today when working in the visual wavelength regime due to its high quantum efficiency

(QE) (that describes how many of the incident photons on the detector surface are registered) and the low read-out noise that is generated by the electronics in the system.

In IFS the needed detector pixels are defined by the wanted spatial sampling and the spectral coverage. If the l, m are the number of spatial resolution elements sought of axes x and y so the number of elements of the grid formed is $l \cdot m$ and the n is the number of spectral elements then the needed number of pixels is $N = l \cdot m \cdot n$. This means that the IFS needs at least a factor of n more detector pixels than are needed in direct imaging where $n = 1$. The total number of detector pixels needed is then

$$\Sigma_{pixels} \geq N_{spaxels} \cdot N_{Spectra}. \tag{10}$$

In general, maximizing the number of spaxels or the available number of spectral pixels is obtained at the expense of the other. However the slicer designs (see later) with precise segmenting can function in a way that this condition is not required. [11]

2.3.2 Lenslet arrays

Lenslet array represents a technique where the the image formed by the telescope is segmented by the lenslets to form separate pupils (practically following a principle that was first used with a "Fabry lens" that is used to reduce noise from seeing in photoelectric photometers [16]). These pupils (or often called micro-pupils) are typically a few tens of micrometers in diameter. As the pupils can be thought to act as a multiple slits with the exception that the configuration is formed by the telescope pupil rather than the telescope image. This results in a light distribution where the slit deficits (as introduced earlier) in terms of wavelength are non-existent leaving the static pupil image unaffected by the atmospheric effects which is important in precision spectroscopy. The segmented pupils are then forwarded into a imaging spectrograph which disperses the light to form adjacent spectra featuring the pupils as spaxels. To avoid spectral overlapping the combination of band width filters (to restrict received light) and rotation between the dispersion axis and lenslet array is required. The rotation is partially done so that more of the detectors surface would be used while the spectral coverage is maximized [11]. The dispersed elements are captured by the a camera that forwards the elements onto a detector aperture such as a CCD. In theory the spatial coverage with the lenslet array can reach 100% allowing the image gathered by the telescope to be sampled contiguously so that spectral information is not lost [15]. The downside of this technique is that the spectrum produced by this method without overlapping of adjacent spectra is

quite limited and it does not take full advantage of the detector surface. The lenslet array technique can provide large number of spaxel with contiguous sampling leading to a high spatial resolution but this must be done with the expense of spectral coverage. The optimal study for this method is one that does not require large wavelength range such as individual absorption lines in galaxies [17]. The concept of the optical layout is shown in Figure 4.

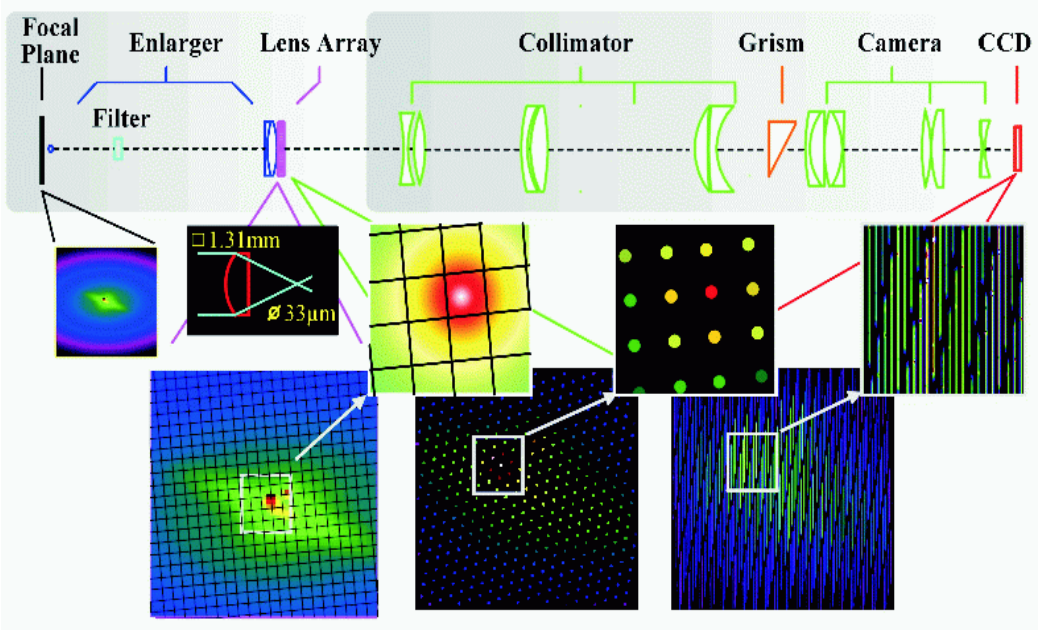

Figure 4: Credit: R. Bacon et al. 2001

2.3.3 Fiber + Lenslet array

Historically the optical fiber system itself represents the first and the most simple technology when it come to IFUs. The optical fibers can be thought as wave-guides that consist of the core of the fiber that is made of high refractive index glass, the cladding as a low refractive index cover enveloping the core and a protective buffer [11]. In the technique the fibers are used to transport the array segmented image from the telescope to the spectrograph. The fibers are aligned to form a pseudo-slit before the gathered light is directed to the spectrograph allowing fast throughoutput and allowing the method to be integrated to already existing spectrographs. Fibers can be used with a lenslet array so that the sampling of the image from a telescope is more contiguous than what is achieved by only using cylindrical fibers for gathering light. In this configuration each fiber is centered on one micro-pupil that is

formed at the exit of the lenslet array plane. Lenslets can be also used on the exit of the fiber to reduce the Focal Ratio Degradation (FRD) (as the FRD is believed to be partly due to inhomogeneities in the fiber and physical roughness of the end-faces where the light enters or exits the fiber [18] as in [11] the FRD is also mentioned to be time-variable due to the possible thermal and mechanical stresses induced on the fiber) which is one of the downsides of the technique [17]. The FRD causes the light cone that is inserted in the fiber to change so that the exiting beam leaves with a larger opening angle than the initially inserted beam. The FRD is able to create noise that in the end can limit the best possible signal-to-noise ratio (S/N) that can be obtained even under the most suitable conditions [11]. Even with a typically low amount of spaxels and the problematic properties as mentioned above (which can be handled with proper care) the fiber concept offers a flexible installation and good wavelength coverage making it a good technique for application that need high spatial resolution [11]. The concept is shown in Figure 5.

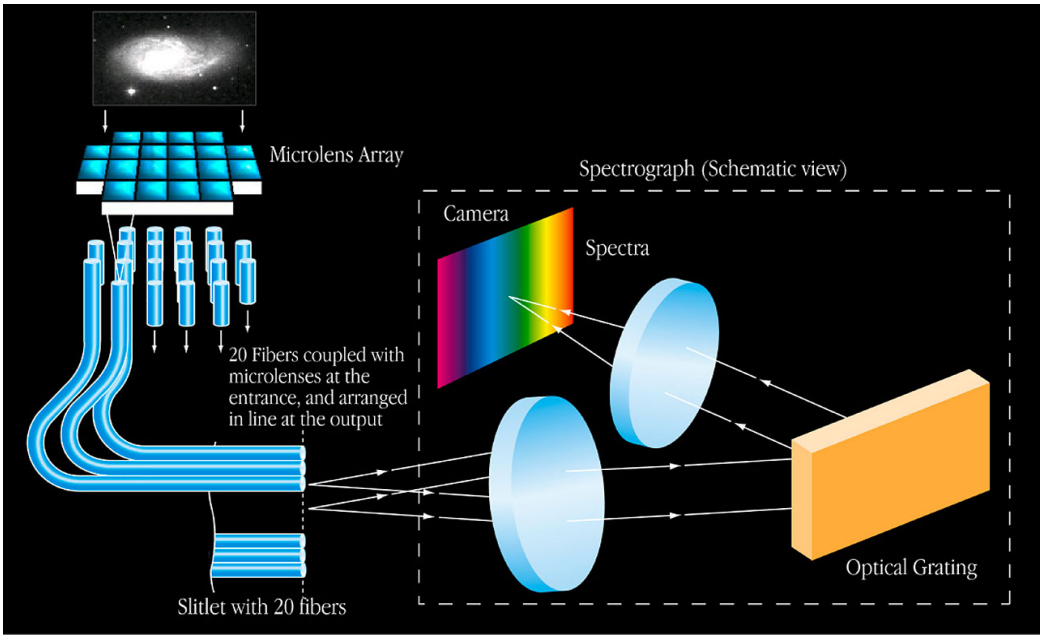

Figure 5: Credit: ESO

2.3.4 Slicer IFUs

The fiber and lenslet array based instruments represent the first generation of IFUs. However the limited number of spaxel in comparison to the direct

imaging and the poor use of the detector surface were drivers for the development of the slicer technique that was presented by [19] (to introduce 3D-technique that would not suffer the time penalty as the Stepped-longslit or FPI, mentioned before, as these were the main techniques applied at the time) [11]. In this method the image from the telescope is directed to a mirror plane. The mirror plane is segmented in slices that are oriented in different angles to divide the image plate into sliced segments. These segments are then gathered into a slit that compose of the separate slices aligned next to each other and form the entrance of the spectrograph. The spectrograph then produces the spectra from the "slits" and images them onto the detector [17]. The configuration allows the imaging of the telescope focal plane directly onto detector so that with a delicate scaling one pixel can be interpreted as one spaxel. This results into the highest packing density on the detector among the IFUs presented here [11]. As the technique uses only mirrors it is optimal for longer wavelength observations where the instruments must be cooled to reduce the thermal background radiation. Also the technique produces a slit and can be thus integrated over existing equipment [17]. A downside is that the manufacturing of the optics might be demanding [13]. The concept is shown in Figure 6.

2.4 Data extraction

Distinctive dynamical processes in a galaxy can be connected to events that describe the evolution and formation of the galaxy. Integral-field spectroscopy is the ideal tool for measuring kinematics in galaxies. By analyzing the kinematics associated with different parts of the galaxy differences between stellar populations are revealed and can be related to different evolution phases [9][10]. The 2D-spectral analysis can be then combined with photo metric observations to form further understanding of the object [20].

Before one can trace the kinematics it is good to know that the instruments do not produce the datacube directly. First the data needs to be reduced and this itself is a subject of its own. The software used on reductions are instrument-based and can include many steps such bias and dark subtraction, extraction of the spectra using a fitted mask model, wavelength calibration, low-frequency flat-fielding, cosmic-ray removal, homogenization of the spectral resolution over the field, sky subtraction and flux calibration. These are mentioned for lenslet array based IFU, SAURON [21].

For the sake of simplicity lets assume we have a final product the datacube shown in Figure 2. For obtaining data that is of interest one needs tools to extract the certain properties from the produced datacube. These tools are programs that fit the spectra acquired from the object in the sky. Most

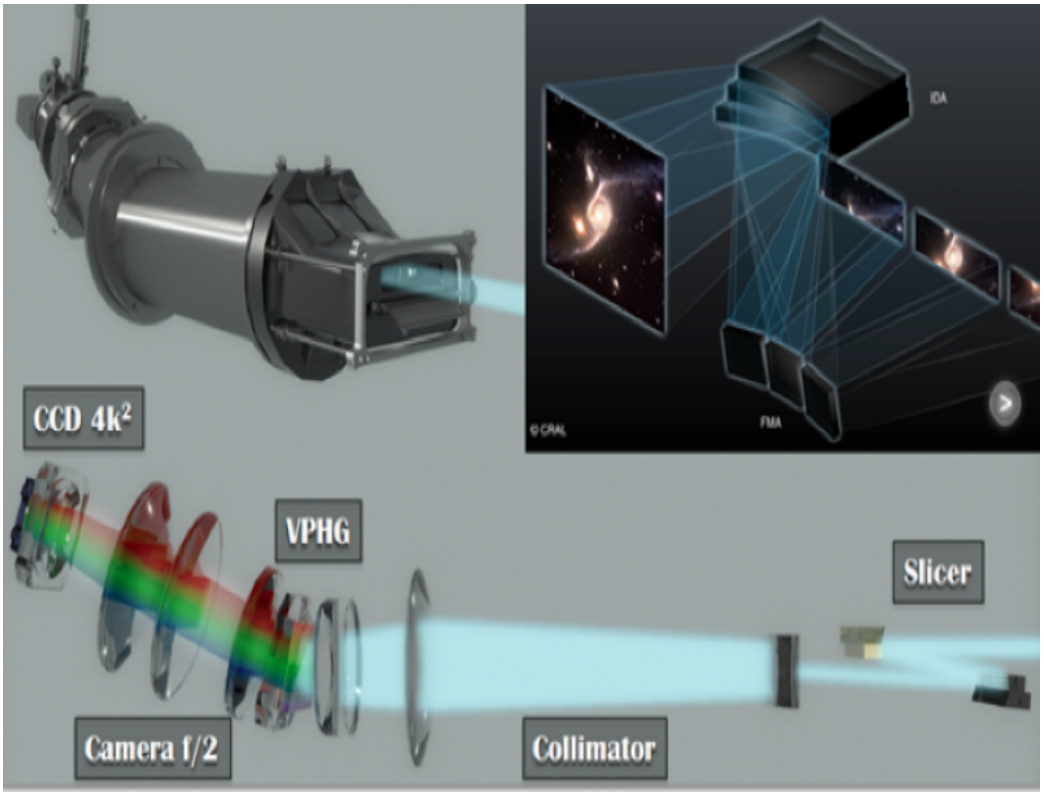

Figure 6: Credit: ESO

of these tools that model stellar populations work with a similar principle. The stellar emission observed is assumed to be a combination of different single stellar populations [22]. By comparing the data with broadened stellar templates the stellar kinematics of the system can be modelled [23].

2.4.1 pPXF

Penalized pixel fitting - pPXF is connecting the observed spectra to large set of stellar templates together with kinematics via full spectrum fitting. The template spectra are convoluted with a Gauss-Hermite expansion in order to reproduce the spectra from the object. The program extracts stellar and gas kinematics as well as the stellar populations from the datacube [23].

2.4.2 FIT3D

FIT3D is a tool for fitting emission lines and the continuum to analyze gaseous emission and stellar kinematics [11]. It was first developed for analyzing spectra from IFS surveys in the optical range by analyzing physical

properties of gas in a system through the emission lines produced by the gas. Since then it has also developed to describe the stellar populations as well. Even though this program was not meant for analyzing kinematics it still give estimates on properties such as stellar velocity and velocity dispersion [22].

3 Presentation of the 2D-data

As the basic concepts of 2D-spectroscopy are discussed above, in this section, the usefulness and visualization power of the technique is displayed by presenting and analyzing actual 2D-data. The aim here is to demonstrate 2D-spectroscopic data obtained with MUSE by presenting kinematic maps of 13 galaxies and further do so by analyzing the sigma-drop phenomenon with radial velocity dispersion profiles. The 2D data is presented by using Python with the package Matplotlib. The radial velocity dispersion profile of each galaxy is obtained by fitting elliptical apertures to the target by eye and with the help of the given position angle (PA) and ellipticity shown in Table 1. The ellipticity is described by flattening by the $\log \frac{a}{b}$ where the a and b are the semi-major and semi-minor axes of the galaxy respectively.

3.1 σ-drop

A σ-drop is a phenomenon where the radial velocity dispersion σ profile, obtained from a galaxy, is observed to drop near the centre of the galaxy. This is counter-intuitive because one would expect the velocity dispersion to increase as the potential minimum of the galaxy is approached. The Sigma-drops appear to be caused by a dynamically cold "star-formation" component fueled by a inflow of gas to the central region of the galaxy. The phenomena seems to be observed more often in galaxies with an active galactic nucleus (AGN) and favored in galaxies that have visible spiral structure that could trace the inflow of material to feed the AGN. The momentum of surrounding gas can be consumed by friction striving the gas to the nuclei. The gas is then closing up until it reaches a critical density and starts collapsing for star formation. As a result the young stars dominate the obtained spectrum with velocity dispersion inherited from the gas which is dynamically colder than the one observed in older stellar populations. Another possibility might be that the area where the sigma-drop is observed is inside of a dark matter halo which then affects the detected velocity dispersion. [24]

The fact that we observe galaxies with flat velocity curves (as mentioned in the thought process earlier) although the luminous mass density decreases

towards the of outer parts of the galaxy, indicates the presence of dark matter [25]. Since the universe contains giant galaxies with inner regions that seem to lack the dark matter that influences the dynamical properties of the galaxies this would indicate that the dark matter can be denser in some regions than others perhaps even at a galaxy scale as in the inner regions of giant galaxies. It is then possible that the observed velocity dispersion of the system could well be affected by presence of a dark matter concentration.

However the star formation still appear to be the more prominent reason for the sigma-drops. As the simulations done on in [26] support the star formation in a cool disc which is formed by inflow of gas to the centre of galaxy leading the dominant younger population in the spectra. The analysis done in [27] on optical and near-infrared datacubes of the central region of NGC1566 seem to show similar results. The kinematic maps extracted with pPXF from a 2D-spectroscopic data obtained with IFU of GMOS (Gemini Multi Object Spectrograph) showed a stellar disk around the AGN of the galaxy that was possibly affecting the emission detected from the AGN with radiation produced by the hot young stars in the stellar disk.

3.2 MUSE

The data used in the practical part of this work were obtained with MUSE. It is a second generation instrument for the Very Large Telescope (VLT) of the European Southern Observatory (ESO). MUSE is a integral-field spectrograph operating in the visible wavelength region. It can use adaptive optics to improve its spatial resolution and covers a large simultaneous spectral range (the data used here was obtained before the installation of the adaptive optics). It is optimized for research at high redshifts (galaxy formation) as well as in the solar system (Galilean satellites, Titan).

MUSE (Multi Unit Spectroscopic Explorer) at VLT that uses image slice technique to sample the area of interest. MUSE splits the field of view (FoV) of 1'(in its wide-field mode) into 24 segments and further dividing each into 48 mini slits with total of 1152 mini slits with sampling of 0.2". MUSE Achieves a spectral resolution of $R = 1750$ at 450nm to $R = 3750$ at 930nm. The narrow-field mode covers 7.5" FoV with a sampling of 0.025". [ESO]

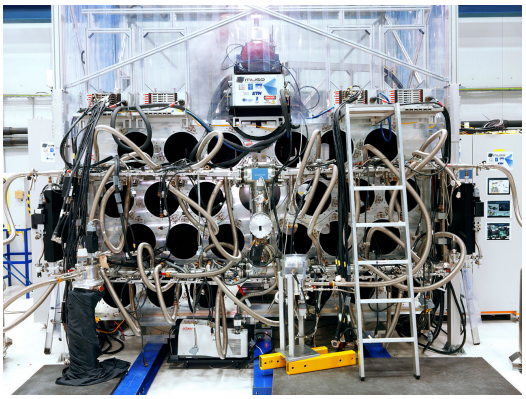

Figure 7: MUSE detectors. ESO

3.3 Specimens

This work involves 13 early type spiral galaxies. The galaxy properties used in this work are listed in Table 1. The properties were obtained from the NASA/IPAC Extragalactic Database (NED) and from the HyperLeda - Database for physics of galaxies (to be marked as HL hereafter). The diameters D of the major axes of the galaxies vary from 17 kpc to 68 kpc with two positive Seyfert AGNs and one possible. Three of the sample galaxies are showing properties that seem to diverge from some of the values obtained from the databases mentioned above. NGC1433 features a position angle (PA) oriented at 87.9°, however, based on the kinematic profiles and the image of the galaxy center the orientation of the central part seems to be at $\approx 32°$. Similar feature can be seen on NGC4643 that shows a central region that is oriented at $PA \approx 45°$ rather than the value of 137.1° listed in HL. This can be seen also in NGC5850 where the corresponding value is $\approx 118.9°$ and part of the central region shows a orientation of the $PA \approx 31°$. Both orientations in these cases were considered. The exact properties used for the radial profile extraction are described in section §3.5.2 and can be found in Table 1 with the rest of the sample properties.

Galaxy	Type	D[kpc]	D["]	PA	$\log a/b$	AGN	Bar
NGC0613	Sbc	45.70	451.90	122.2°	0.09	Seyfert?	B
NGC1097	SBb	67.62	812.83	133.9°	0.21	LINER	B
NGC1433	SBa	22.19	480.00	$87.9°_{(32.3)}$	$0.32_{(0.09)}$	-	B
NGC3351	Sb	24.65	510.00	10.7°	0.21	-	B
NGC4643	S0-a	23.21	186.31	$131.7°_{(45.0)}$	$0.11_{(0.13)}$	-	B
NGC4984	S0-a	17.07	165.31	36.4°	0.13	-	B
NGC5339	Sa	24.87	114.31	69.1°	0.09	-	B
NGC5728	Sa	29.86	203.20	11.1°	0.19	Seyfert 1.9	B
NGC5806	Sb	22.70	189.70	171.8°	0.27	Seyfert 2	B
NGC5850	Sb	27.20	300.00	$118.9°_{(31.0)}$	$0.15_{(0.12)}$	-	B
NGC7140	SABb	52.64	360.00	17.4°	0.17	-	B
NGC7421	Sbc	24.77	184.08	80.6°	0.09	-	B
NGC7552	Sab	17.07	305.49	$-(0°)$	0.04	-	B

Table 1: Properties of the galaxies in the sample. The () indicates the alternative value tested

3.4 Elliptic aperture

A simple elliptical aperture is used to obtain the radial velocity dispersion profiles from the data. This approach should be good in cases where the sigma-drop might inhabit areas that might be missed by a slit-aperture and for the fact that the ellipse-aperture accounts for the inclined nature of the objects. Errors are bound to exist just by the assumption of the "symmetry" of the object. The interactions with bars could affect symmetry of the system and the PA might not stay constant throughout the disk of the galaxy deviating from the PA obtained according to a larger scale (as can be seen on the NGC1433). The same argument can be applied to the observed inclination of the object as the observed central region can be decoupled from the larger scale inclination of the galaxy. The initial centering of the aperture was done by eye with the help of the kinematic maps (see Figure 8 for further details). The used aperture elements ($\log \frac{a}{b}$ and PA) are the ones shown in the Table 1.

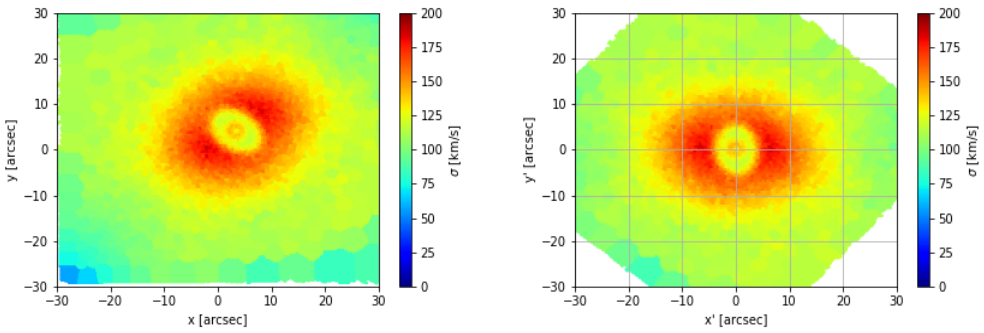

Figure 8: Showing the initial centering of the aperture

The aperture uses the given axis ratio to determinate the ellipticity based of flattening

$$\epsilon = \sqrt{1 - \frac{b^2}{a^2}} \tag{11}$$

The galaxies are oriented in different angles in the sky thus the PA needs to be accounted for while extracting the wanted information from the given data. Here the basic coordinate transformation for a coordinate system that is rotated by an angle ϕ is applied

$$\begin{cases} x' = x\cos\phi - y\sin\phi \\ y' = y\cos\phi + x\sin\phi \end{cases} \tag{12}$$

where the x, y are the coordinates from the given data. For a value of r, that describes the radial distance in a galaxy, the data points within this radius for flattened system in a rotated frame can be given with a ellipse equation

$$\frac{x'^2}{a^2} + \frac{y'^2}{b^2} = \frac{x'^2}{r^2} + \frac{y'^2}{(1-\epsilon^2)r^2} \leq 1 \tag{13}$$

where the x', y' are the coordinates of the transformed system. The equation is then used as a boolean indexing to get the desired coordinates with the corresponding velocity dispersion values from the velocity dispersion maps between consecutive radial values.

By considering the 1 arc-minute FoV of MUSE the array elements (used to extract the radial profiles from the velocity dispersion data of the galaxies) are chosen to consist of 20 linearly-spaced bins in the range of [0, 40]" resulting into a 2" radii covered by a single aperture section. This leads to high amount of elements in a single bin which should give a accurate average velocity dispersion value in the area but leads to decrease in the spacial precision of the description of the sigma-drop. Nevertheless the amount of data points should allow a more precise method but for at first order of accuracy the aperture used here should function correctly and provide information worth of demonstration and simple analysis.

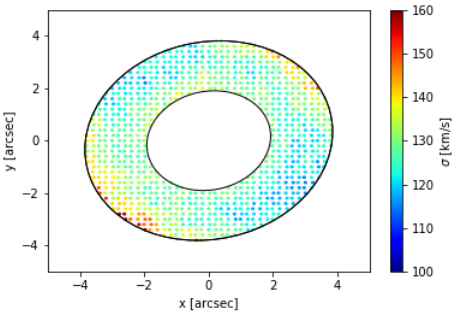

Figure 9: Demonstrating the data included within a bin.

After obtaining the points between consecutive array elements, of the given radial array, the velocity dispersion values are then averaged within a bin and standard deviations are recovered for plotting radial profile with error bars as first-order accuracy indicators.

3.5 Profiles

The aperture extracted profiles are shown with the corresponding kinematic maps plotted from the given data and can be found as an appendix at the end of this work. The properties of the sigma-drops as obtained from the radial velocity dispersion profiles are shown in Table 2.

3.5.1 Radial measurements

The width σ_{size} (radii covered by the sigma-drop) of the sigma-drop here is defined as the distance from the point where the velocity dispersion starts to decay (measured towards the center) to the point where the same local maximum value is reached again or the center of the galaxy is encountered. The minimum velocity dispersion value is used to determine the radial location σ_{drop} of the sigma-drop. The magnitude of the drop $\Delta\sigma$ is measured from the point of decay to the minimum (measured towards the center). The position of the sigma-drop relative to the size of the galaxy is measured by dividing the sigma-drop position with the half diameter $D/2 = \alpha$ of the galaxy. As the extraction of the sigma-drop properties is done in 2" aperture segments these are plotted so that the extracted value would be at the middle of the 2" segment, in other words, the extracted average radial velocity dispersion value within the first 2" in a galaxy is plotted so that it is located at 1" rather than 0" or 2" from the center of the galaxy and so on.

3.5.2 NGC1433, NGC4643 and NGC5850

The radial profiles of NGC1433 are obtained with two separate elliptic aperture fits corresponding the PA obtained from HL with value of $PA = 87.9°$ and the one resulting from a fit based on the kinematic maps and the image of the galaxy. In the fit value of $PA = 32.3°$ is adapted as this seems to be the favored orientation of the inner region of the galaxy. However by taking a closer look at the inner regions of the galaxy there also appear to be observable difference in the $\log\frac{a}{b}$, decoupling from the one in HL, that is showing a different inclination of the inner region in the galaxy. In the fitting process the axis-ratio is observed to be $\log\frac{a}{b} = 0.09$ showing more face-on orientated inclination as the "database-value" is $\log\frac{a}{b} = 0.32$. In the end both "corrections" are chosen to be applied in the alternative radial profile extraction. Significant change can be seen in the radial profile with the alternative elliptic aperture orientation. The radial profile shows less standard deviation close to the sigma-drop with the $PA = 32.3°$ and $\log\frac{a}{b} = 0.09$ orientation parameters possibly indicating more accurate values for the gathered radial properties. Ultimately the location of the sigma-drop stays the same as the most obvious distinction can be made in the width of the sigma-drop with ≈ 8" separation between the two different aperture orientations. Clearly the alternative aperture orientation here is justified.

The kinematic maps and the image of the center regions of NGC4643 show similar features. The orientation-parameters of the galaxy, according to HL, are $PA = 131.7°$ and $\log\frac{a}{b} = 0.11$ as the very center region seems to

be oriented at $PA = 45.0°$ and $\log \frac{a}{b} = 0.13$. The radial profiles extracted do not show as "dramatic" differences as in the case of NGC1433 but still there is some change that can be noticed. The standard deviations of the radial profile of NGC4643 also appear to favor the alternative aperture orientation close to the sigma-drop region. Yet the alternative aperture properties in this case, result only in a relatively small change of the $\Delta\sigma$.

In NGC5850 the optional orientation of the central region can be seen as well but unlike the two galaxies before the rotation velocity map of the galaxy does not seem to favor the alternative orientation (as one would expect the highest rotation velocity to be seen at the ends of the semi-major axis). On the other hand the velocity dispersion and h_4 maps of the galaxy are showing possible orientation that is diverging from the properties in HL. The very center of the galaxy seems to inhabit a "ring" with $PA = 31.0°$ and a more face-on axis-ration of $\log \frac{a}{b} = 0.12$ as the listed properties are $PA = 118.9$ and $\log \frac{a}{b} = 0.15$. The alternative orientation results into small standard deviations closer to the sigma-drop as this was also the case with the two galaxies above. Here two of the sigma-drop properties are changing between the two aperture orientations. The listed orientation results to two points that denote the σ_{drop} in the radial profile (average is taken) while the optional parameters lead to a single point defining the minimum with steeper curve resulting larger $\Delta\sigma$. Also the width of the sigma-drop is observed to change.

As the properties of the sigma-drops obtained with both aperture orientations are shown in the Table 2, the average of these (if there is observed change) is used in the results later on. These "case-based" radial profiles can be found as an appendix with rest of the sample. The top ones corresponds to the profiles based on the values in HL and under those are the ones with the alternative orientation (in cases where the alternatives were considered).

3.5.3 NGC7521, NGC613 and NGC3351

The most peculiar profile belongs to galaxy NGC7421. Based on the profiles of the galaxy there seems to be a possible sigma-drop at the very center of the galaxy as well as a "mega" sigma-drop covering most of the FoV with relatively low $\Delta\sigma$. The central sigma-drop can be seen on the kinematic map corresponding the velocity dispersion of the galaxy but is barely standing out in the radial profile (except maybe as a slight drop or flattening effect) which is probably due to the chosen aperture size. The larger sigma-drop can be seen well on the radial profile of the galaxy. The large size of the sigma-drop with a poorly defined minimum (that is used to define σ_{drop}) with $\Delta\sigma \approx 5$km/s causes the extraction of accurate position of the sigma-

drop to be rather difficult with the methods used here. Eventually the σ_{drop} is taken roughly from the radial distance located at halfway of the measured σ_{size} corresponding the width of the drop. The value obtained through this method is then used in the result section.

A Similar flattening effect (as mentioned in the case of NGC7421 on the observed radial velocity dispersion profile) can be seen on NGC613 and NGC3351. On the radial profile of NGC613 it appears as if there might be a secondary sigma-drop in the very center of the galaxy, however, in this case the image and kinematic maps of the galaxy can be used to further analysis. The image shows very strong visible dust structures going to the center parts of the galaxy that could be causing the features seen on the profiles. It would seem as if the dust features would be also "merging" with the morphology of the observed sigma-drop in the velocity dispersion map of the galaxy. In [24] they mention the possibility of dust structures tracing the material flow to the inner parts of the galaxy that fuels the sigma-drop phenomenon.

On NGC3351 the sigma-drop morphology on the kinematic maps of the galaxy also appear to be following features shown on the image of the galaxy. A bright stellar ring that is accompanied by dust arms around the central region of the galaxy as well as a possible stellar disk (towards the center from the stellar ring) can be seen on the kinematic maps of the galaxy (or rather the connection between these can be made). Similar features can be also seen in NGC1097 which shows a very strong stellar ring that can be connected to the kinematic maps. The puzzling thing at the first sight is that the dust lanes seem to "merge" with the features that are shown with higher velocity dispersions in the kinematic maps! But assuming that the kinematic maps correspond to the detected stellar spectra lead to a conclusion that the younger stellar population forming in a dense ring of inflow material (that the dust ring traces) with lower σ are partly obscured by the dust and the possibly older population with higher σ that are not obscured by the dust dominate the spectral features in those parts. This then results in a local increase in the observed velocity dispersion profile where the dust features are present. This would also make sense since the features in the velocity dispersion maps (that seem similar to the dust structures) possess the same velocity dispersion as the "outer-inner" regions of the galaxies that possibly compose of the bulge stars.

Thus the flattening of the radial profile in both of the cases does not appear to be caused by a secondary sigma-drop but rather "spiral-features" of dust close to the centre of the galaxy. The dust lanes connect the "main" sigma-drop that is probably caused by a dynamically-cold stellar component and conceal part of the stellar flux from the sigma-drop region of the galaxy.

The connection between the visible dust lanes and the observed sigma-

drop morphology in the kinematic maps seems to be present in all of the sample galaxies that show a visible dust structure in the central regions. One could wonder if the sigma-drop would be caused by the dust then (as if one would look a very edge-on galaxy the velocity dispersion would drop at the disk level and rise when moving perpendicular to the disk), however, at least two galaxies (NGC1097 and NGC3351) seem to show a bright stellar "ring" tracing these features (as said earlier). These star-burst features could be formed by shock-focusing of the gas due to the interaction with bars that force the inflow of gas into a dynamically-cold ring around the central region of the galaxy. The ring is then packed until a critical density is reached triggering the star formation and ultimately causing the detected sigma-drop [24][28]. The sigma-drop morphology on the velocity dispersion maps can be clearly connected with the bright stellar rings accompanied by the dust features seen on these galaxies. As the sigma-drops can be detected also in the galaxies that lack the visible dust lanes, appear to act as a further confirmation of the phenomenon being rather stellar-induced than a feature caused by just the dust lanes extending to the central regions of galaxies. One might still argue if the dust alone could be the cause of some of the sigma-drops in the observed profiles. The lonely dust features (lacking strong SF indices) could possibly be connected with the sigma-drop phenomenon as a pre-star-burst phase where the stars are forming and the dust is covering the underlying stellar component resulting mainly "dust-caused" sigma-drop. The dust could act as a cover that blocks the flux from stellar components with the highest σ close to the potential minimum of the galaxy resulting a spectra that shows stellar components with a lower σ surrounding the very central regions and ultimately a sigma-drop. If the dust was indeed covering "intense" star formation it could be probably seen as relatively high far-infrared (FIR) emission as this can be related to the SFR [29].

3.5.4 Results & Discussion

The radial profiles obtained from the sample of 13 possible sigma-drop galaxies seem to indicate that every galaxy in the sample hosts a sigma-drop. The sigma-drops are observed to inhabit within the inner 5% of the semi-major axis (obtained from NED) in most of the sample galaxies. The exception of this is found in two of the sample galaxies NGC7421 and NGC4984 in the case of NGC7421 this is probably due to the nature of the profile obtained. The average radial distance covered by the sigma-drops and the average radial position of the sigma-drop in the sample are (1.1 ± 0.6)kpc and (0.7 ± 0.8)kpc respectively. The main reason (or rather the culprit) for the high deviations seem to be due to the NGC7421 where the radial profile

of the galaxy shows a sigma-drop that covers a area larger than half of the FoV with poorly defined features as explained earlier. The average amplitude of the sigma-drops observed in the sample is (21.7 ± 11.3)km/s.

The deviations in the σ_{size} , $\Delta\sigma$ and σ_{drop} show a broad variety that indicates the individuality of the sigma-drops. One would naturally expect that the measured attributes are to be changed as the galaxy properties such as size changes. For example in [28] a star-formation ring in the central region of a galaxy (that is believed to be the cause of the sigma-drops) is connected with a bar driven inner Lindbland resonance (ILR) forming a molecular ring around the central region of the galaxy. ILR then shocks and compresses the gas and thus increases the star-formation in the vicinity. As the mass of a bulge in a galaxy is increased it would lead to a higher rotation velocities of surrounding gas enlarging the radius of the ILR. This can be then connected to a galactic evolution (where the star-formation ring starts at small radii and is pushed outward) as the bulge mass increases over time, as thought in [28], or possibly to the properties of different galaxies in same evolution "phase" where more massive galaxies could possibly present more extensive star-formation ring features. These could be partially seen as an explanation for the observed divergence in the sigma-drops here, however, in this sample there seems to be no direct connection between the size of the galaxies and the radial size or radial location of the sigma-drops which is in an agreement with [24]. The latter can be seen from Figure 10.

As there is no control sample that could be used as reference the favoring of a sigma-drop in a galaxy with an AGN (as both phenomenon can be connected with increased inflow of gas [24]) cannot be noted. The sample does include few galaxies with a sigma-drop and an AGN (4 based on HL and 6 on NED), however, the majority of the galaxies in this sample do not have AGNs. As this is not showing if the sigma-drop are favored in the galaxies with AGN or not but it seems to be showing that as for the existence of the sigma-drop the AGN is not required. The possible reason is that the life-time of the sigma-drops is considerably longer and it can outlive the period of the activity of the AGN gradually relaxing as the inflow of matter stops. The long life-time of the drops could partially explain the large deviations seen in the sample as the sizes of the sigma-drops would change over the time [24].

Even without the presence of reference data few morphological aspects are worth mentioning. Firstly all of the galaxies in the sample are classified as barred galaxies (based on HL). The bars indeed could be the drivers for the inflow of gas towards the central regions [30]. The inflow material then forms a ring due to the bar induced IRLs that "shock-trigger" the star formation in the ring. This is eventually detected as a sigma-drop in the spectra caused by the dynamically cold stellar component near the centre of

the galaxy. Secondly many of the galaxies seem to have visible inner dust spiral structure towards the central region as this was also preferred in the sigma-drop galaxies over the control sample galaxies in [24]. The fraction of "dust trailed" galaxies in the sample here is roughly 70% indicating a firm correlation between the sigma-drops and the dust. The galaxies that lack the dusty structure are NGC4643, NGC5339, NGC5850 and NGC7421. This can be seen as confirmation of that the dust is not the main cause of the sigma-drops but it could well be accompanied by a evolution of one (by tracing the possible inflow of gas [24] and by possibly showing increased FIR emission due to the increasing SFR in the vicinity [29]).

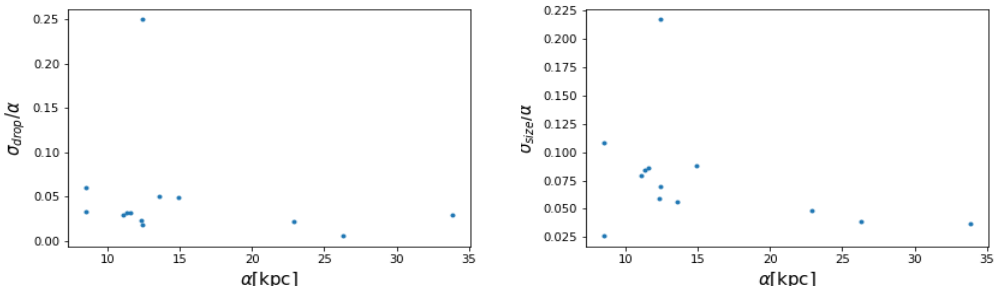

Figure 10: Correlation of the σ_{drop} and σ_{size} with the galaxy sizes

Galaxy	σ_{drop}[kpc]	σ_{drop}/α	σ_{size}[kpc]	$\Delta\sigma$[km/s]
NGC0613	0.5	0.02	1.1	15
NGC1097	1.0	0.03	1.3	40
NGC1433	0.3(0.3)	0.03(0.03)	1.1(0.7)	30(35)
NGC3351	0.3	0.02	0.7	25
NGC4643	0.4(0.4)	0.03(0.03)	1.0(1.0)	35(40)
NGC4984	0.5	0.06	1.0	20
NGC5339	0.2	0.02	0.9	10
NGC5728	0.7	0.05	1.3	35
NGC5806	0.4	0.03	1.0	20
NGC5850	0.7(0.6)	0.05(0.05)	0.8(0.7)	15(20)
NGC7140	0.2	0.006	1.0	20
NGC7421	3.0	0.3	2.7	5
NGC7552	0.3	0.03	0.2	5

Table 2: The measured sigma-drop properties

4 Discussion & Conclusion

The basic concepts of the 2D-spectroscopy in astronomy were covered with potential room for more extensive research on the subject. The most effective technique for extracting the data that is needed to do the scientific analysis seems to be the "slicer" technique with low information loss due to the sampling of the focal plane directly onto the detector plane leading to the highest packing density of the detector. As on [13] it is mentioned that the number of the needed detector pixels dominates the hardware cost of the instruments.

The scientific motivation for the 2D-dimensional spectroscopic techniques is demonstrated through the kinematic maps showing various possibilities for the surveys where the spatially resolved spectrum is required. The analysis of the sigma-drop sample used here shows a single application for the use of the 2D-spectroscopic data. The results obtained in this demonstration are in an agreement with the ones in the [24] with one exception. The sigma-drop position in the galaxy NGC1097 (that happens to be the also included in the sample used in this work) in [24] is listed to reside at $r_{drop} = 4$" and in this work the value obtained is closer to a 12". The decision on what is used as the point defining the sigma-drop could well explain the difference but in [24] it is also mentioned that in several papers (from where they obtained the used sigma-drop values) the sigma-drop was measured only along one axis and does not thus provide as good results as IFU spectroscopy.

The connection between the σ-drop phenomenon and a dynamically-cold stellar component can be made. The feature could be formed by bar-driven IRLs that push the inflow of gas to circumnuclear ring and "shock-trigger" the SF. The visible dust structures, seen on the galaxies here, seem to trace the inflow of gas to the sigma-drop site as they "merge" with the morphology of the σ-drops in the kinematic maps of the galaxies.

2D spectroscopy seems to be becoming an ever more powerful tool in a astronomical research-kit. The possible application for the spatially resolved spectra are ranging from the very early universe to the present-day solar system. It offers a fresh perspective on how the astrophysical problems can be tackled and ultimately how the nature is perceived. The basic principles behind 2D-spectroscopy in astronomy discussed here are only a scratch on the surface in the topic and thus leave room to be explored. Clearly some the possibilities can be seen from the demonstration done here. The simple way of applying a two-dimensional aperture to a system that is projected on a two-dimentional surface for obtaining certain physical properties and visualizing the kinematics in the system is already itself a presentation of the capabilities of the integral field spectroscopy.

References

[1] J. F. James. *A Student's Guide to Fourier Transforms : With Applications in Physics and Engineering.*, volume 3rd ed. Cambridge University Press, 2011.

[2] Frederick R. Chromey. *To Measure the Sky : An Introduction to Observational Astronomy.* Cambridge University Press, 2010.

[3] Arthur Beiser. *Concepts of modern physics.* McGraw-Hill, New York, N.Y., sixth edition, international edition edition, 2003.

[4] Kenneth R. Lang. *The Life and Death of Stars.* Cambridge University Press, 2013.

[5] Brad K. Gibson, Yeshe Fenner, Agostino Renda, Daisuke Kawata, and Hyun-chul Lee. Galactic Chemical Evolution. , 20(4):401–415, Jan 2003.

[6] Hale Bradt. *Astronomy Methods : A Physical Approach to Astronomical Observations.* Cambridge University Press, 2004.

[7] Jeanna Buldyreva, Nina Lavrentieva, and Vitaly Starikov. *Collisional Line Broadening And Shifting Of Atmospheric Gases: A Practical Guide For Line Shape Modelling By Current Semi-classical Approaches.* Imperial College Press, 2011.

[8] Linda S. Sparke. *Galaxies in the universe : an introduction.* Cambridge University Press, Cambridge, 2nd ed edition, 2007. Lisäpainokset: Repr. 2007.

[9] E. Emsellem, R. Davies, R. McDermid, H. Kuntschner, R. Peletier, R. Bacon, M. Bureau, M. Cappellari, Y. Copin, B. Miller, E. Verolme, and T. de Zeeuw. Probing the Stellar Populations of Early-Type Galaxies: the SAURON Survey (Invited Talk). In M. Rosada, L. Binette, and L. Arias, editors, *Galaxies: the Third Dimension*, volume 282 of *Astronomical Society of the Pacific Conference Series*, page 189, January 2002.

[10] R. M. McDermid, R. Bacon, H. Kuntschner, E. Emsellem, K. L. Shapiro, M. Bureau, M. Cappellari, R. L. Davies, J. Falcón-Barroso, D. Krajnović, R. F. Peletier, M. Sarzi, and T. de Zeeuw. Stellar kinematics and populations of early-type galaxies with the SAURON and OASIS integral-field spectrographs. , 49:521–535, January 2006.

[11] E. Mediavilla. *3D Spectroscopy in Astronomy.* Canary Islands Winter School of Astrophysics. Cambridge University Press, 2010.

[12] MS Westmoquette, KM Exter, L Christensen, M Maier, M Lemoine-Busserolle, J Turner, and T Marquart. The integral field spectroscopy (ifs) wiki. *arXiv preprint arXiv:0905.3054*, 2009.

[13] Jeremy Allington-Smith. Basic principles of integral field spectroscopy. *New Astronomy Reviews*, 50(4):244 – 251, 2006. Integral Field Spectroscopy: Techniques and Data Production.

[14] Gyula P Szokoly. Optimal slit orientation for long multi-object spectroscopic exposures. *Astronomy & Astrophysics*, 443(2):703–707, 2005.

[15] R. Bacon, G. Adam, A. Baranne, G. Courtes, D. Dubet, J. P. Dubois, E. Emsellem, P. Ferruit, Y. Georgelin, G. Monnet, E. Pecontal, A. Rousset, and F. Say. 3D spectrography at high spatial resolution. I. Concept and realization of the integral field spectrograph TIGER. , 113:347, October 1995.

[16] J. Michlovic. Optical activities in industry. *Applied Optics*, 11(2):490–492, 1972.

[17] J. Allington-Smith and R. Content. Sampling and Background Subtraction in Fiber-Lenslet Integral Field Spectrographs. , 110:1216–1234, October 1998.

[18] Colin Dunlop, Graham Murray, Ulrike Lemke, and Jeremy Allington-Smith. End effects in optical fibres. *Monthly Notices of the Royal Astronomical Society*, 436(4):3492–3499, 10 2013.

[19] L. Weitzel, A. Krabbe, H. Kroker, N. Thatte, L. E. Tacconi-Garman, M. Cameron, and R. Genzel. 3D: The next generation near-infrared imaging spectrometer. , 119:531–546, November 1996.

[20] R. L. Davies, H. Kuntschner, E. Emsellem, R. Bacon, M. Bureau, C. M. Carollo, Y. Copin, B. W. Miller, G. Monnet, R. F. Peletier, E. K. Verolme, and P. T. de Zeeuw. Galaxy Mapping with the SAURON Integral-Field Spectrograph: The Star Formation History of NGC 4365. , 548:L33–L36, February 2001.

[21] E. Emsellem, M. Cappellari, R. F. Peletier, R. M. McDermid, R. Bacon, M. Bureau, Y. Copin, R. L. Davies, D. Krajnović, H. Kuntschner,

B. W. Miller, and P. T. de Zeeuw. The SAURON project - III. Integral-field absorption-line kinematics of 48 elliptical and lenticular galaxies. , 352:721–743, August 2004.

[22] S. F. Sánchez, E. Pérez, P. Sánchez-Blázquez, J. J. González, F. F. Rosález-Ortega, M. Cano-Dí az, C. López-Cobá, R. A. Marino, A. Gil de Paz, M. Mollá, A. R. López-Sánchez, Y. Ascasibar, and J. Barrera-Ballesteros. Pipe3D, a pipeline to analyze Integral Field Spectroscopy Data: I. New fitting philosophy of FIT3D. , 52:21–53, April 2016.

[23] M. Cappellari. Improving the full spectrum fitting method: accurate convolution with Gauss-Hermite functions. , 466:798–811, April 2017.

[24] S. Comerón, J. H. Knapen, and J. E. Beckman. On the morphology of sigma-drop galaxies. , 485:695–705, July 2008.

[25] Edvige Corbelli and Paolo Salucci. The extended rotation curve and the dark matter halo of m33. *Monthly Notices of the Royal Astronomical Society*, 311(2):441–447, 2000.

[26] E. Portaluri, V. P. Debattista, M. Fabricius, D. R. Cole, E. M. Corsini, N. Drory, A. Rowe, L. Morelli, A. Pizzella, and E. Dalla Bontà. The kinematics of σ-drop bulges from spectral synthesis modelling of a hydrodynamical simulation. , 467:1008–1015, May 2017.

[27] J. E. Steiner, Patrícia da Silva, and R. B. Menezes. NGC 1566: analysis of the nuclear region from optical and near-infrared Integral Field Unit spectroscopy. *Monthly Notices of the Royal Astronomical Society*, 470(4):3850–3876, 06 2017.

[28] T. Böker, N. M. Forster-Schreiber, and R. Genzel. Near-Infrared Imaging Spectroscopy of IC 342: Evolution of a Bar-Driven Central Starburst. , 114:1883, November 1997.

[29] Louis Martinet and Daniel Friedli. Bar strength and star formation activity in late-type barred galaxies. *arXiv preprint astro-ph/9701091*, 1997.

[30] L. Lin, C. Li, Y. He, T. Xiao, and E. Wang. Bar-induced central star formation as revealed by integral field spectroscopy from califa. *Astrophysical Journal*, 838(2), 2017.

NGC613

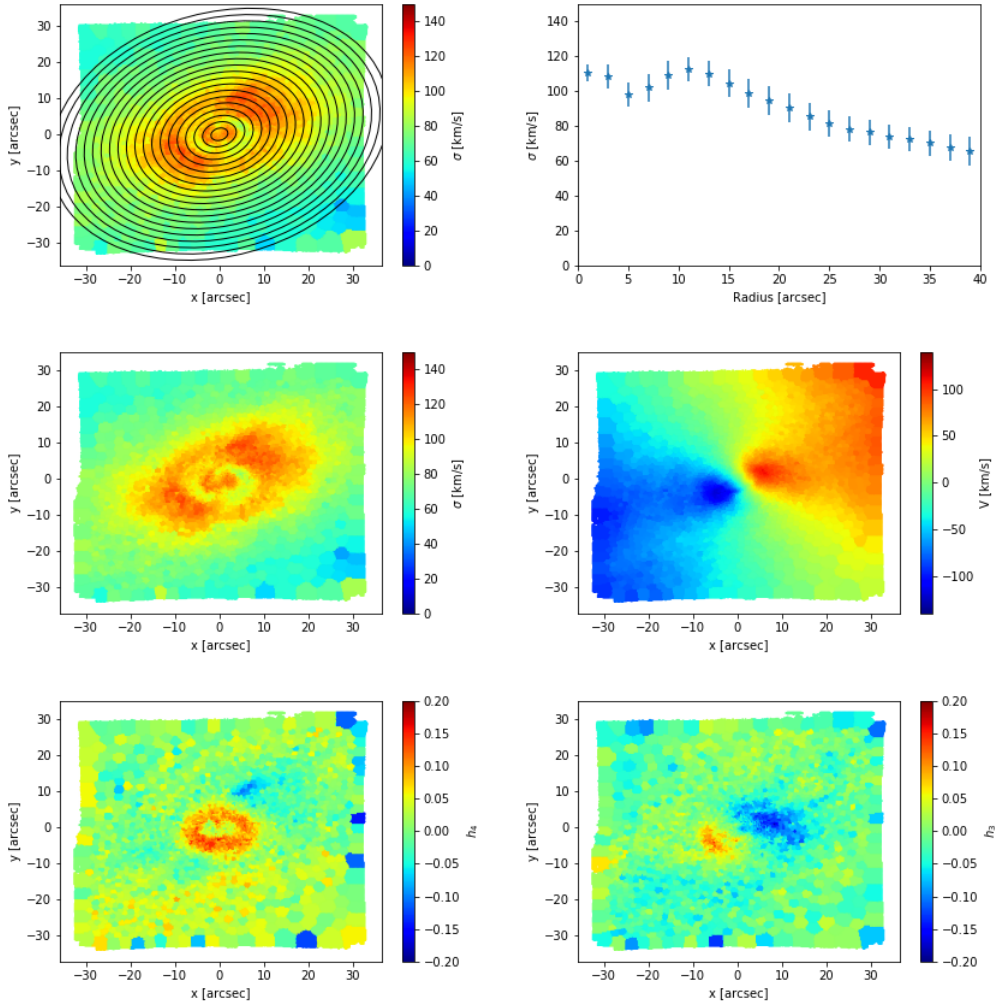

Figure 11: Kinematics and the radial velocity dispersion profile. Top: Left elliptical aperture, right the radial profile. Middle: Left the velocity dispersion profile, right the rotational velocity profile Bottom: Symmetric and asymmetric line of sight velocity dispersion (LOSVD) deviation from a Gaussian with amplitudes h_4 and h_3 of the Gauss-Hermite series. Left (h_4) showing the symmetric deviation, right asymmetric (h_3)

NGC1097

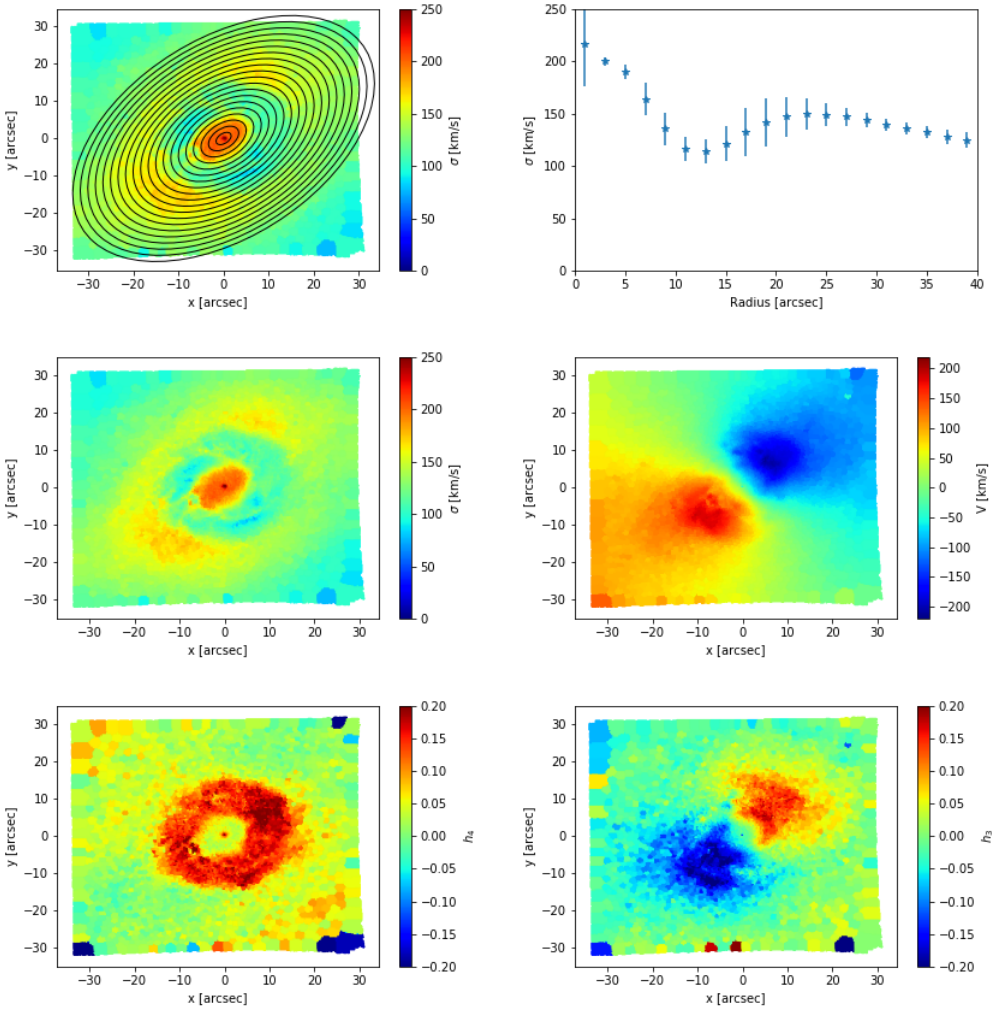

NGC1433

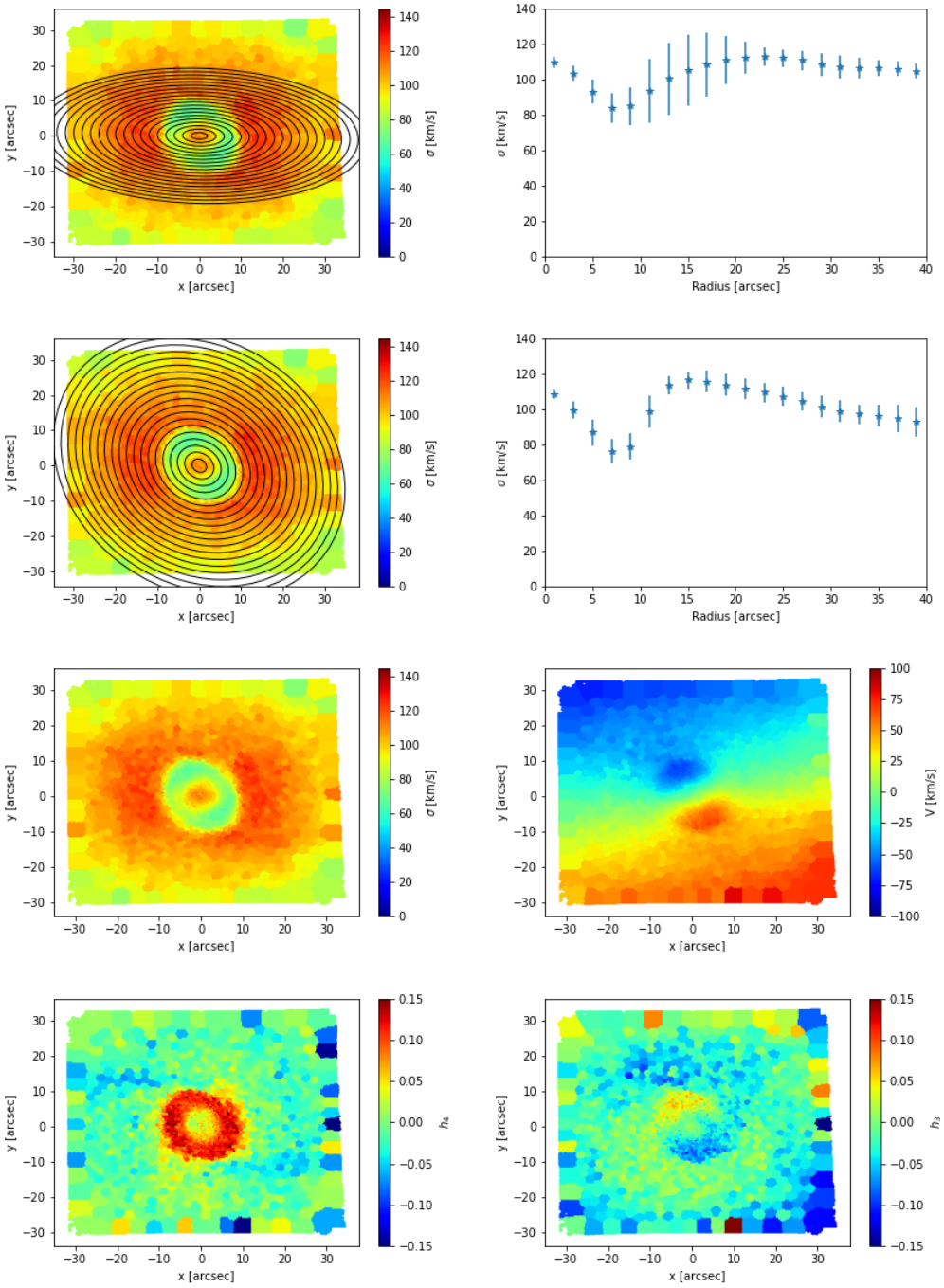

NGC3351

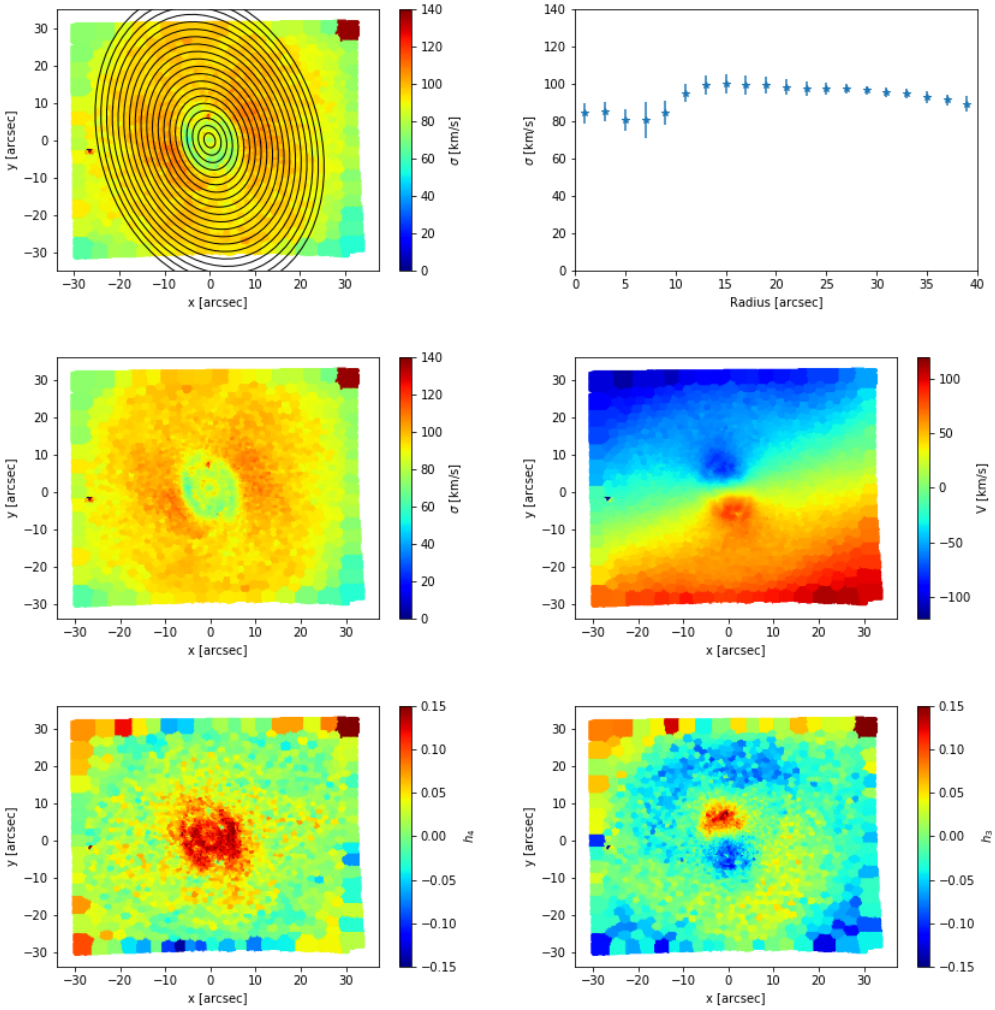

NGC4643

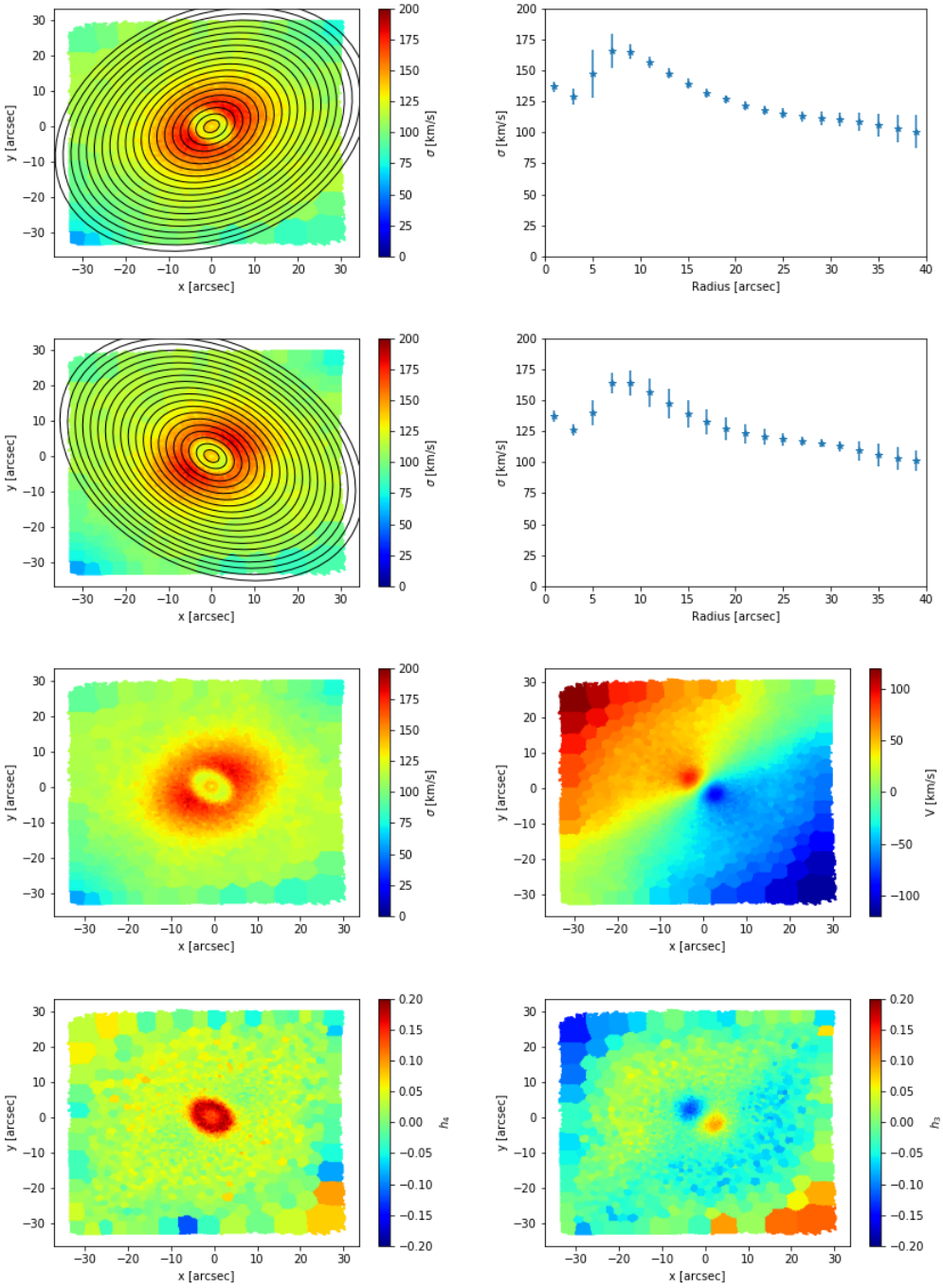

NGC4984

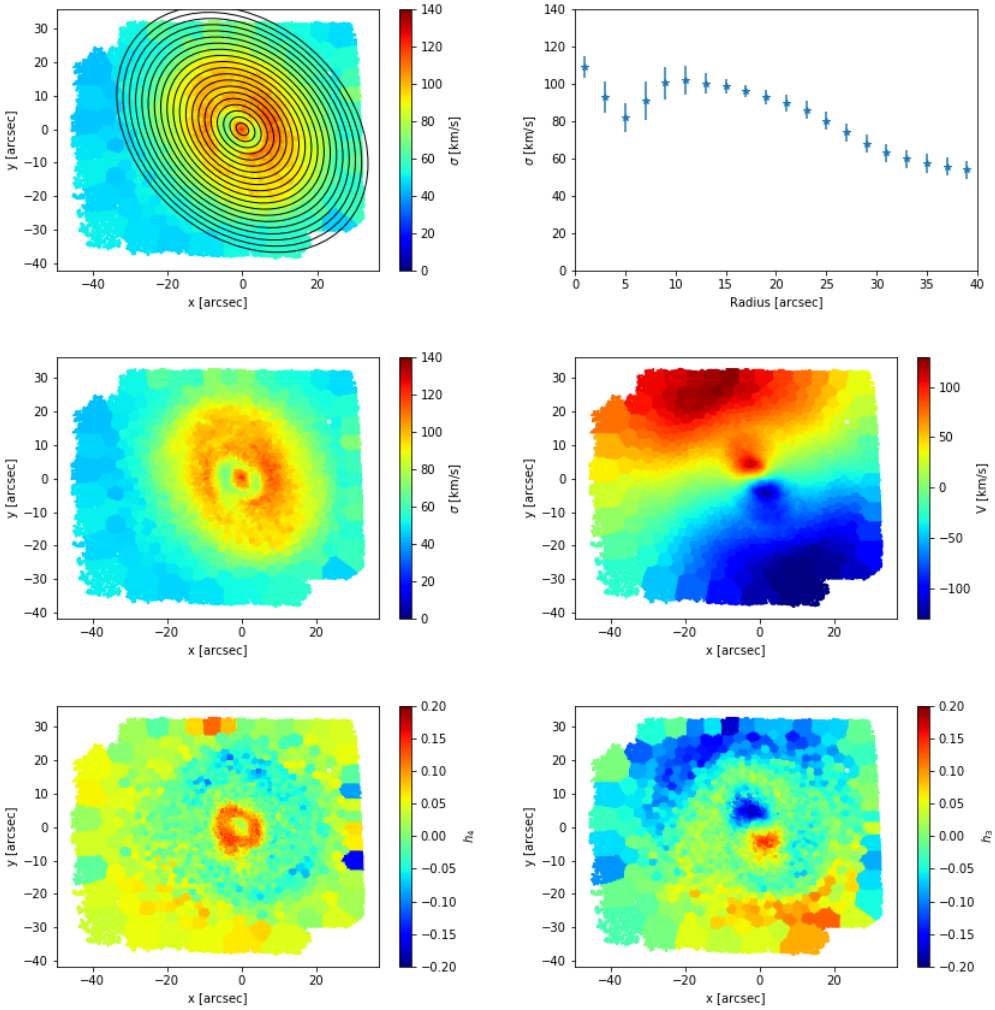

NGC5339

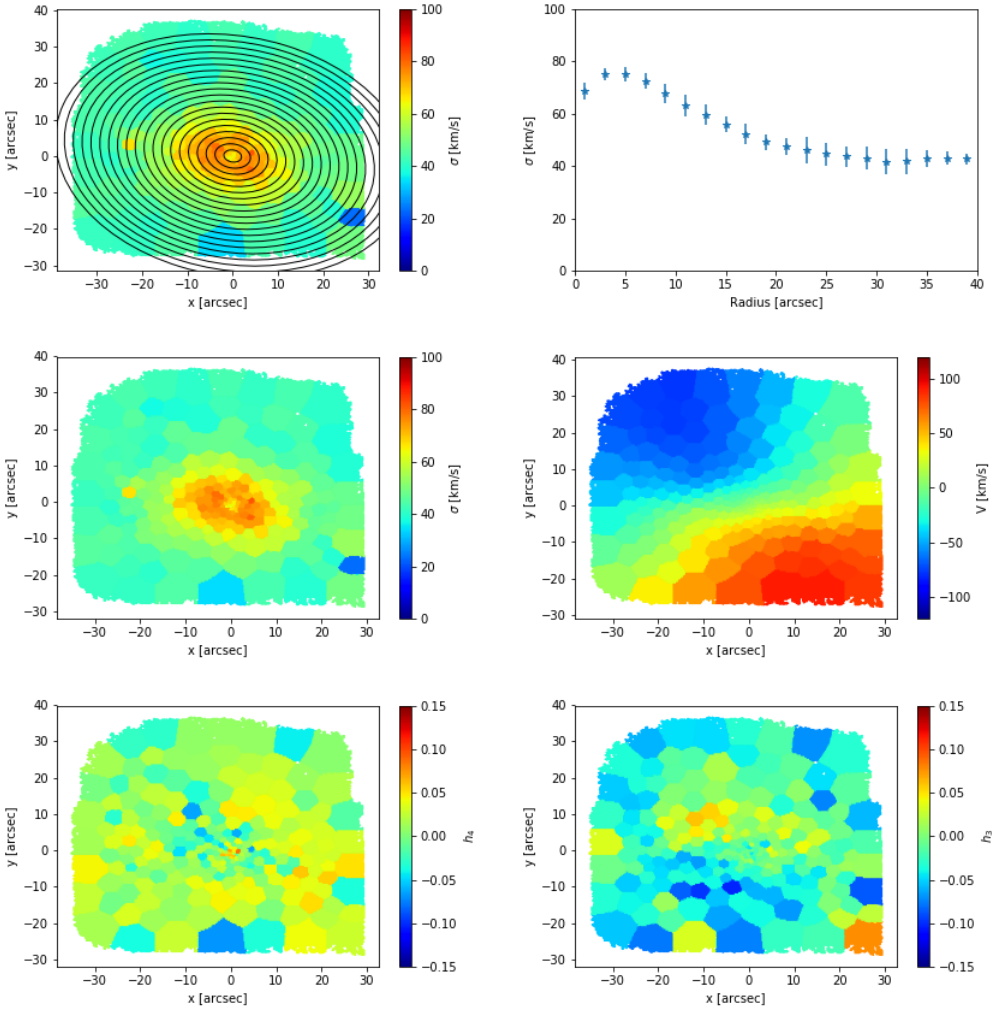

NGC5728

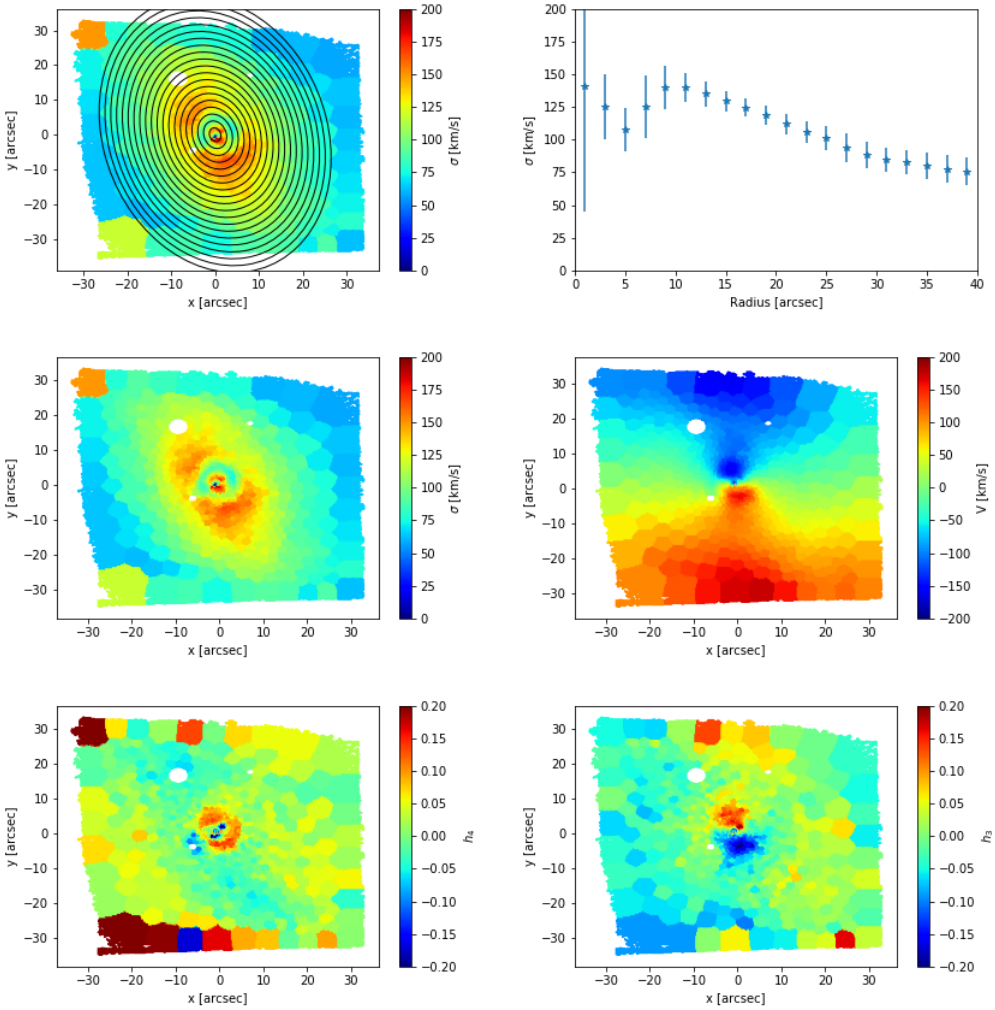

NGC5806

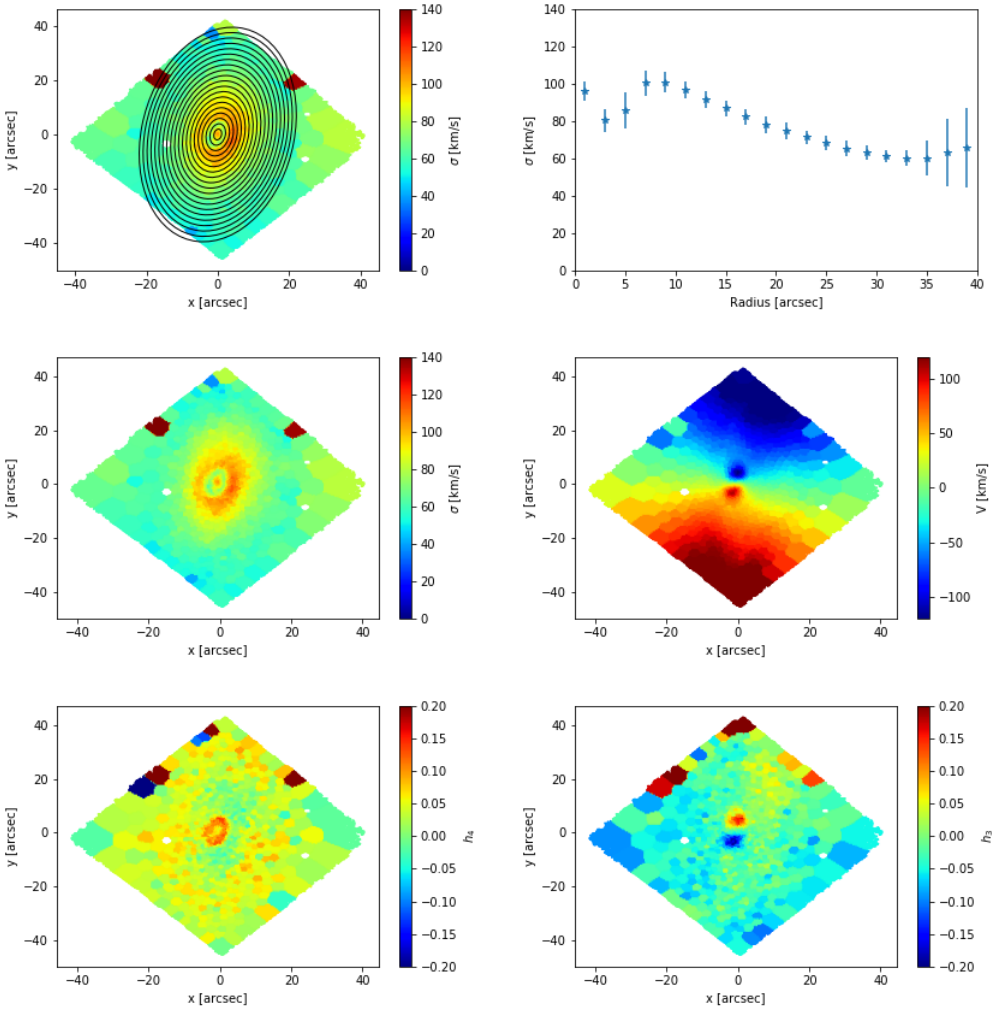

NGC5850

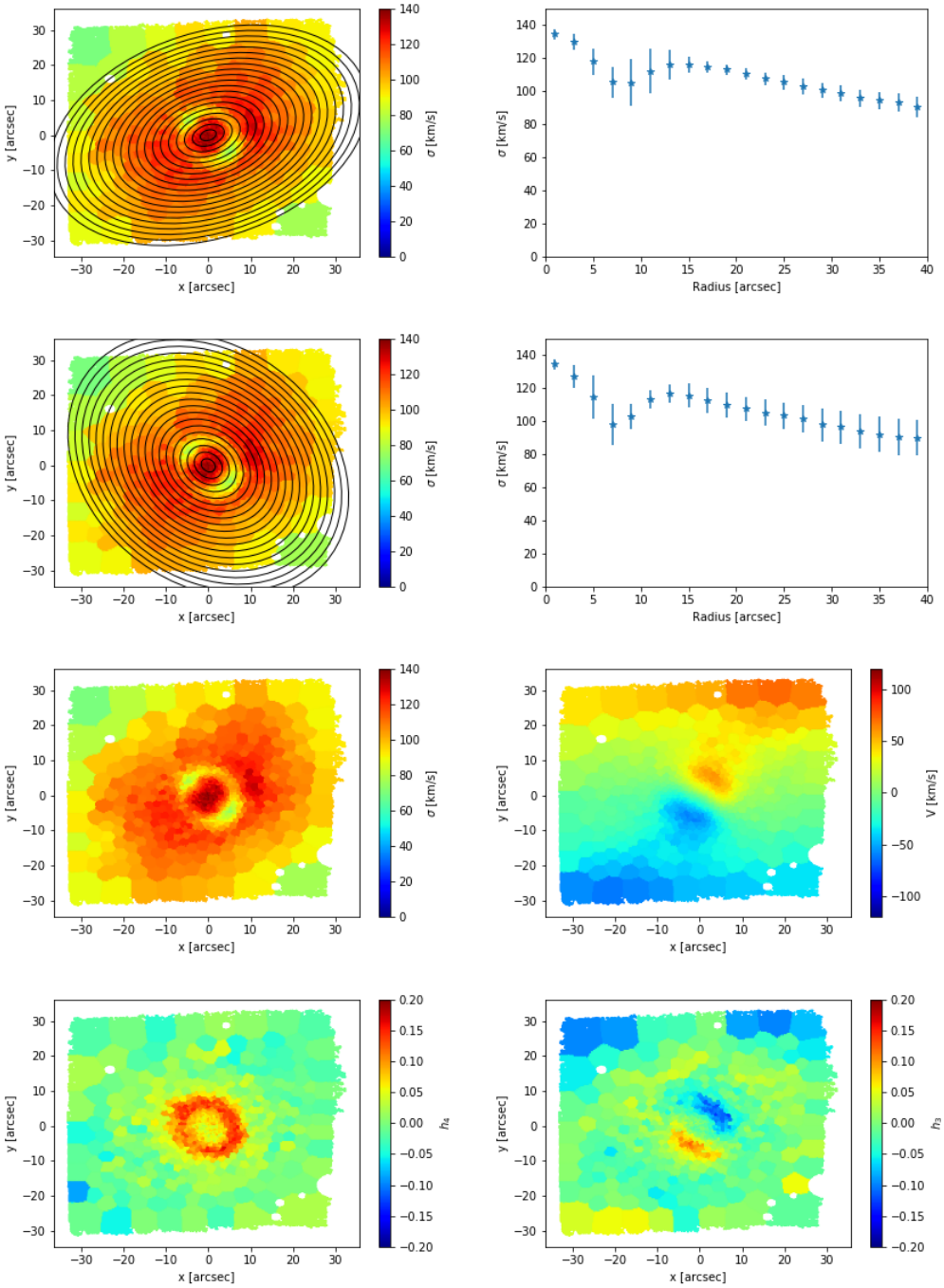

NGC7140

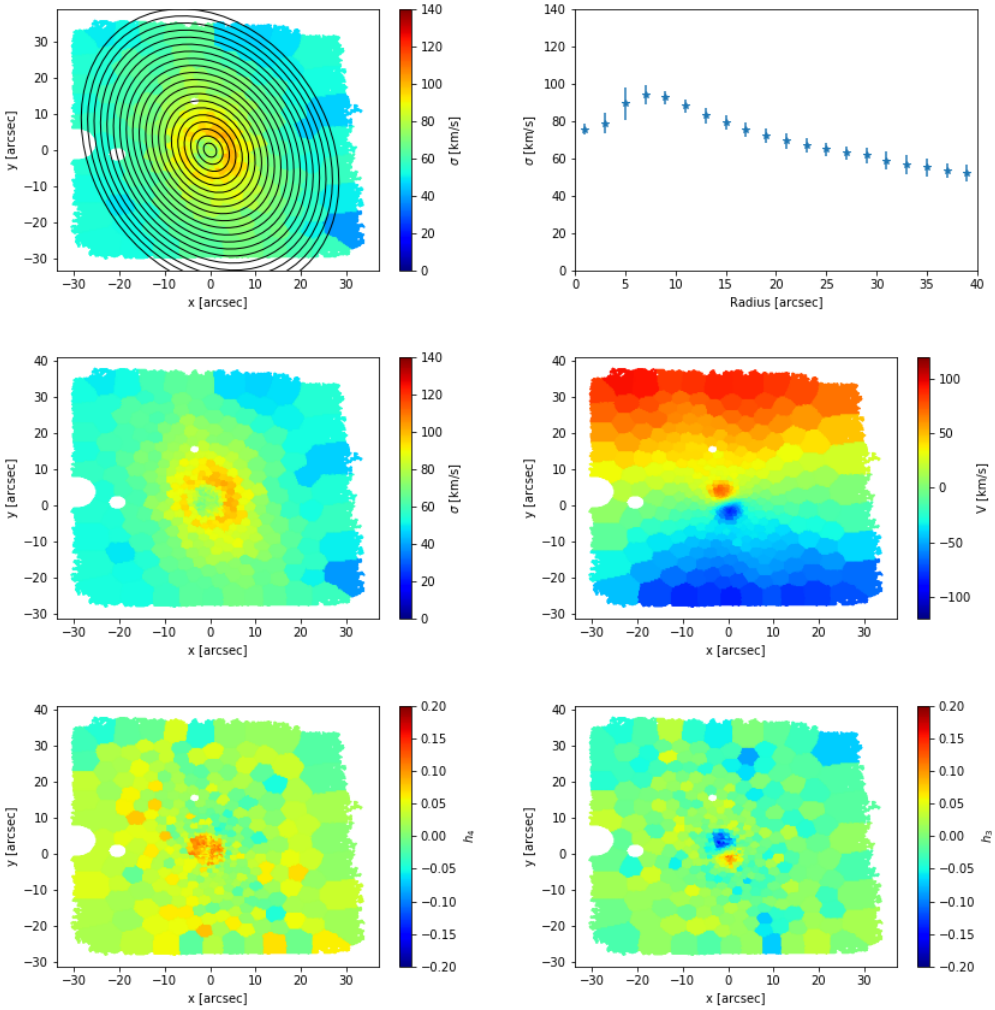

NGC7421

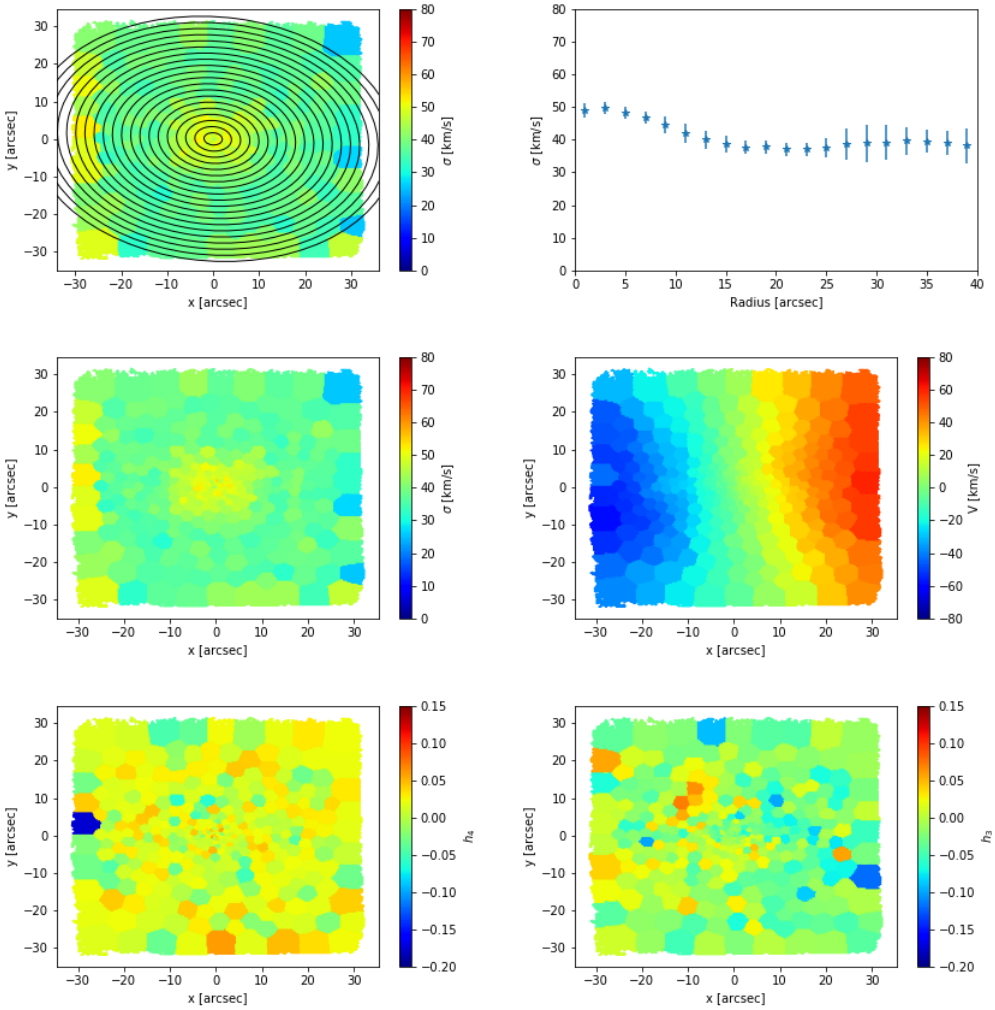

NGC7552